Mineralogical, geochemical, and textural indicators of crystal accumulation in the Adamello Batholith (Northern Italy)

Author(s):
Fiedrich, Alina M.; Bachmann, Olivier; Ulmer, Peter; Deering, Chad D.; Kunze, Karsten; Leuthold, Julien

Publication date:
2017-12-01

Permanent link:
https://doi.org/10.3929/ethz-b-000216500

Originally published in:
The American Mineralogist 102(12), https://doi.org/10.2138/am-2017-6026

American Mineralogist, Volume 102, pages 2467–2483, 2017

Mineralogical, geochemical, and textural indicators of crystal accumulation in the Adamello Batholith (Northern Italy)

Alina Maraike Fiedrich[1,*], Olivier Bachmann[1], Peter Ulmer[1], Chad D. Deering[2], Karsten Kunze[3], and Julien Leuthold[1]

[1]Department of Earth Sciences, ETH Zurich, 8092 Zurich, Switzerland
[2]Department of Geological and Mining Engineering and Sciences, Michigan Technological University, Houghton, Michigan 49931, U.S.A.
[3]Scientific Center for Optical and Electron Microscopy, ETH Zurich, 8093 Zurich, Switzerland

Abstract

In this study, we quantitatively investigate crystal-melt segregation processes in two upper-crustal, intermediate-to-silicic plutons from the Tertiary Adamello Batholith, Italian Alps, by combining (1) an estimation of the amount of crystallized interstitial liquid using cathodoluminescence images, phase maps, and mass-balance calculations with (2) quantification of crystal preferred orientation using electron backscatter diffraction. Cathodoluminescence images, phase maps, and plagioclase profiles are used together to distinguish early grown primocrysts from overgrowths formed after the rheological "lock-up" of the magma bodies. Mass-balance calculations, taking into account mineral compositions and bulk-rock chemistry, are used as an additional means to quantify the amount of trapped melt. The following features are indicative of crystal accumulation (or melt loss) in some parts of the batholith: (1) The amount of crystallized interstitial liquid can be low and negatively correlated with crystal (and shape) preferred orientations. Locally, up to ca. 27% melt may have been lost. (2) Significant intracrystalline deformation in plagioclase (up to ca. 13° of lattice distortion) is present in strongly foliated samples, resulting from compaction in a highly crystalline mush. These mineralogical and textural features indicative of variability in the degree of crystal accumulation in some areas of the Adamello batholith may explain the highly scattered bulk-rock geochemical patterns (particularly in trace elements). However, the precise quantification of the amount of melt loss remains challenging in felsic plutons, because of the compositional deviation from liquid lines of descent due to multi-scale variations in the degree of crystal-melt segregation and the fact that magmatic textures indicative of crystal accumulation can be subtle.

Keywords: Adamello, crystal cumulate, crystallized interstitial liquid, intermediate-to-silicic batholith, phase maps, cathodoluminescence

Introduction

Research interest

Melt extraction from intermediate-to-silicic crystal mush has been the topic of numerous studies to explain the origin of crystal-poor rhyolites (e.g., Bacon and Druitt 1988; Hildreth and Fierstein 2000; Hildreth 2004; Bachmann and Bergantz 2008; Deering and Bachmann 2010; Huber et al. 2012). Most of these studies concentrated on the volcanic products, without clearly linking them to the plutonic record. Yet, the latter retains a more complete (time- and composition-wise) record of the magma reservoir dynamics (see recent publications by Miller and Miller 2002; Turnbull et al. 2010; Paterson et al. 2011; Tappa et al. 2011; Beane and Wiebe 2012; Coint et al. 2013; Gutiérrez et al. 2013; Putirka et al. 2014; Graeter et al. 2015; Lee and Morton 2015; Barnes et al. 2016) and can provide important information on the physical mechanisms involved, if any melt segregation has occurred.

Melt segregation can be traced by investigating the crystal cumulates left over after melt separation (e.g., Weinberg 2006; Deering and Bachmann 2010). However, the existence of cumulates in intermediate-to-silicic igneous rocks in the mid- to upper crust is still strongly debated (Bartley et al. 2006; Streck and Grunder 2007; Reubi and Blundy 2009; Deering and Bachmann 2010; Tappa et al. 2011; Davis et al. 2012; Mills and Coleman 2013; Gelman et al. 2014; Streck 2014; Glazner et al. 2015; Lee and Morton 2015; April 2016 issue of *Elements*). If felsic cumulates do not exist, the generation of eruptible melt pockets from shallow, evolved crystal mush, or at least the mechanisms behind it, would be in question. Alternatively, the presence of a significant trapped melt component would render the cumulate signature very subtle (e.g., Gelman et al. 2014).

The presence of cumulates in plutonic lithologies may be recorded by the bulk geochemical signature. For example, as concentrations of incompatible trace elements must increase along the liquid line of descent, the greater the melt loss, the stronger the depletion in incompatible trace elements in the final bulk-rock composition. Strong variability in trace element concentrations within a single differentiation series has been reported from individual plutons all over the world (e.g., Lee and Morton 2015; Walker et al. 2015; Eddy et al. 2016), and part of this variability may be related to crystal-melt segregation. However, identification of cumulates utilizing such bulk-rock techniques suffers from the fact that multiple liquid lines of descent can occur in a single magmatic series, in particular for incompatible elements or

* E-mail: alina.fiedrich@erdw.ethz.ch

0003-004X/17/0012–2467$05.00/DOI: http://dx.doi.org/10.2138/am-2017-6026

elements strongly affected by crustal assimilation, and plutonic lithologies may be compositionally heterogeneous on decimeter to meter scale (coarse-grained lithologies, local melt movement). Hence, to improve our ability to identify the presence of possible intermediate-to-silicic cumulates, investigations should be extended from analysis of bulk-rock geochemical patterns to quantification of the amount of trapped liquid, which correlates inversely with the amount of melt extraction, and identification of textural indicators of compaction and/or crystal settling (in part summarized in Meurer and Boudreau 1998a; for further references see text below). All three methods complement each other when coupled and provide the most complete image of crystal-melt segregation.

Previously applied methods to target the trapped liquid

Minerals in magmas grow in a continuum from free-floating crystals in a dominantly liquid environment to interstitial crystals trapped in the pore spaces of highly crystalline mushes. The trapped liquid represents this later phase, originating after the magma has reached the rheological lock-up (ca. 50 vol% crystals, i.e., solid crystal network forms in 3D: Vigneresse et al. 1996; Petford 2003; Dufek and Bachmann 2010). Estimation of the amount of trapped liquid has been attempted for several magmatic systems by means of bulk-rock geochemistry and trace element modeling in mafic rocks (e.g., Bédard 1994; Meurer and Boudreau 1998a and references therein; Tegner et al. 2009; Leuthold et al. 2014) and in silicic rocks (e.g., McCarthy and Groves 1979; Deering and Bachmann 2010; Gelman et al. 2014; Lee and Morton 2015). The accuracy of such trace element based models depends on the choice of partition coefficients and/or starting compositions, which can vary significantly in many cases. Partition coefficients and the modal mineralogy can vary as a function of pressure, temperature, and melt composition (Blundy and Wood 2003; Forni et al. 2016; although, time-integrated partition coefficients can be internally estimated with high confidence, e.g., Otamendi et al. 2016), while starting compositions cannot be assumed to be perfectly constant nor precisely determined, especially in large magmatic provinces. In addition, averaging of many samples is required to obtain partition coefficients representative for a large plutonic body, but this also impedes the study of variability across the pluton.

Other techniques that have been utilized to estimate the amount of trapped liquid focused more on mineralogical and textural constraints. For example, Graeter et al. (2015) utilized energy-dispersive X-ray spectroscopy (EDS) compositional maps to determine phase proportions and the amount of low-anorthite (An) overgrowth rims on plagioclase in felsic plutonic rocks. Several studies applied cathodoluminescence (CL) imaging to visualize phase proportions (Higgins 2016) and stages of growth in minerals such as quartz or feldspar (e.g., Wiebe et al. 2007; Müller et al. 2010; Götze 2012; Vasyukova et al. 2013; Frelinger et al. 2015). Furthermore, CL is commonly combined with other tools such as crystal size distributions (Higgins 2016), quantitative trace element analysis (e.g., Müller et al. 2003; Słaby et al. 2016), or geochemical modeling (Słaby and Götze 2004) to elucidate the crystallization history. Ginibre et al. (2002, 2007) and Perugini et al. (2005) applied combined backscatter electron (BSE) imaging and electron probe microanalysis to reconstruct the conditions that gave rise to different growth zones in feldspars, thereby providing an alternative method to determine overgrowth rims. In all cases, variations within units can be explored, and the results can be coupled with textural information. However, separating "cores" (crystals that were formed in a largely liquid environment) from "rims" (parts of the crystals that grew from trapped liquid in the pore space) of crystals remains challenging, as multiple variables (e.g., temperature, water content, pressure, degree of differentiation) can have an effect on the compositional parameters (e.g., anorthite content in plagioclase).

Cumulate textures are frequently reported from mafic to ultramafic rocks (e.g., Wager 1960; Brothers 1964; Hunter 1996; Namur and Charlier 2012) but only rarely in intermediate-to-silicic rocks (e.g., Lee and Morton 2015). This is likely due to the higher viscosity of the evolved magma, which leads to a less efficient separation between crystals and melt (Bachmann et al. 2007). Additional factors may be the cooling rate, the relative density difference between crystals and melt, crystal size, and crystal shape (e.g., Brothers 1964). Possible textural indicators of crystal accumulation and melt segregation are magmatic foliation (e.g., Brothers 1964; Hunter 1996; Meurer and Boudreau 1998b, 1998a, their Table 2; Namur and Charlier 2012), intracrystalline deformation (Hunter 1996; Philpotts et al. 1996; Meurer and Boudreau 1998b; Philpotts and Philpotts 2005), and crystal clusters ("synneusis": Vance 1969; Schwindinger and Anderson 1989; Philpotts et al. 1998, 1999; Jerram et al. 2003; Beane and Wiebe 2012; Graeter et al. 2015).

Several ways to quantify the development of these types of igneous textures have been developed (e.g., Launeau and Robin 1996; Meurer and Boudreau 1998b; Launeau et al. 2010). Recently, improvement of the electron backscatter diffraction (EBSD) systems has enabled rapid crystal orientation mapping (Wheeler et al. 2001). Crystal preferred orientation (CPO) is now commonly quantified based on orientation data from EBSD measurements by means of the "J-index" (Bunge 1982; Ben Ismaïl and Mainprice 1998) or the "misorientation (M)-index" (Skemer et al. 2005; Mainprice et al. 2014). Here, CPO and shape preferred orientation (SPO) are equivalent, but for simplicity and because EBSD measures crystal orientations, we use the term "CPO" to describe both CPO and SPO in the following.

Purpose of this study

Transcrustal igneous systems featuring evolved, upper-crustal crystal mushes still defy our understanding (see recent reviews in Bachmann and Huber 2016; Cashman et al. 2017). In an effort to determine, if the origin of the large scatter observed in many bulk-rock geochemical data sets for plutonic systems is related to variability in the efficiency of crystal-melt separation, we assessed cumulate characteristics in carefully chosen lithologies of the Adamello batholith. Phase maps from energy-dispersive X-ray spectroscopy (EDS) scans and cold-cathode CL images were obtained to determine the amount of trapped liquid in different parts of the batholith. The results were compared with those from trace element mass-balance calculations, as performed in Leuthold et al. (2014).

Crystal orientations and crystal deformation measured with EBSD were used to characterize and quantify fabrics, which could be further used to determine the underlying magmatic processes. In particular, we focused on identifying crystal-liquid separation mechanisms that might have occurred and are likely to fall into one or several of the following categories:

(1) hindered settling (Davis and Acrivos 1985; Bachmann and Bergantz 2004; Beane and Wiebe 2012; Lee and Morton 2015), (2) compaction (McKenzie 1984, 1985; Shirley 1986; Philpotts et al. 1996; Jackson et al. 2003; Bachmann and Bergantz 2004; Philpotts and Philpotts 2005), (3) micro-settling (Miller et al. 1988), and (4) gas-driven filter-pressing (Anderson et al. 1984; Sisson and Bacon 1999; Bachmann and Bergantz 2006; Pistone et al. 2015). In a nutshell, we applied a range of techniques to determine whether evidence for crystal-melt segregation in intermediate-to-silicic plutonic systems is preserved.

Geological setting

The Adamello batholith is a ca. 42 to 31 Ma (Del Moro et al. 1983b; Mayer et al. 2003; Schaltegger et al. 2009) Alpine intrusion (Brack 1983), located in the Southern Alps of Northern Italy (Fig. 1a). It intruded into crystalline basement of the Southern Alps and the Permo-Mesozoic cover sediments (Brack 1983) and is wedged between the Periadriatic (Insubric) fault system (Fig. 1a; Laubscher 1983). Paleo-intrusion pressure is less than 3.5 kbar (Thompson et al. 2002; Pennacchioni et al. 2006 and references therein). Today, the batholith is well exposed over an area of ca. 670 km^2 and shows >2 km of vertical relief. The dominant rock types are tonalite and granodiorite (Brack 1983). Potential hints to volcanic activity related to the Adamello batholith are rare and ambiguous (Boyet et al. 2001; Martin and Macera 2014).

Emplacement of the plutons of the Adamello batholith in the upper crust occurred incrementally (see, e.g., separation of units by sharp contacts in Fig. 1; Schaltegger et al. 2009; Schoene et al. 2012; Floess and Baumgartner 2015) and under predominantly

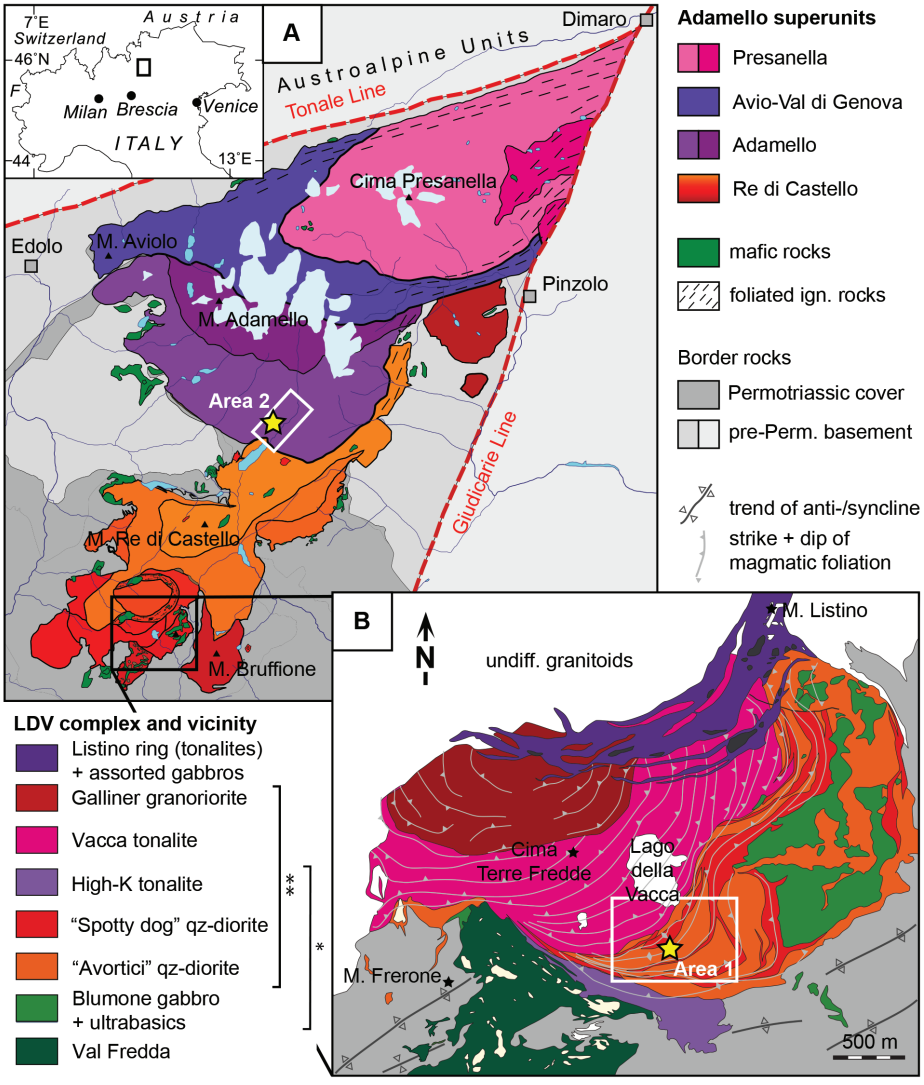

Figure 1. (**a**) The four superunits of the Adamello batholith, wedged between the Tonale and Giudicarie lines. Simplified geological map after Schaltegger et al. (2009), modified from Schoene et al. (2012). (**b**) The Lago della Vacca complex with its four main units Val Fredda, Blumone (including the "Avortici" and "Spotty Dog" batches), Vacca, and Galliner. Simplified geological map with foliation orientations after John and Blundy (1993), modified from Schoene et al. (2012). Sampling locations are indicated with yellow stars. * Blumone Complex after Brack (1983) and Ulmer et al. (1983); ** Lago della Vacca Suite after John and Blundy (1993). Sampling areas indicated with rectangles. (Color online.)

extensional tectonic conditions (Brack 1983; Callegari 1983; Laubscher 1983). The plutons originated from a mantle-derived, Mg-tholeiitic to high-Mg basaltic parental magma (Ulmer et al. 1983; Bigazzi et al. 1986; Kagami et al. 1991; Hürlimann et al. 2016) that underwent progressive crustal assimilation and fractional crystallization (AFC; Taylor 1980). Fractionation followed a calc-alkaline, I-type trend (Macera et al. 1983), which is typical for subduction-related magmas. Geologically and lithologically similar occurrences of composite batholiths are known from most continental arcs and are summarized in Lipman and Bachmann (2015).

The Adamello batholith sensu lato consists of four composite plutons (also referred to as superunits) decreasing in age from southwest to northeast (Del Moro et al. 1983b; Callegari and Brack 2002): Re di Castello (including Corno Alto), Adamello (including the Western Adamello Tonalite, WAT), Avio-Val di Genova, and Presanella (Fig. 1a). The homogeneity and volume of batches increase with decreasing age of intrusion (compare to Fig. 1a; for WAT: Floess and Baumgartner 2015), possibly indicating progressive heating of the crust, while the mantle source may vary slightly (Macera et al. 1983; Hürlimann et al. 2016). Progressive heating is accompanied by an apparent increase in assimilation with time, which is indicated by higher $^{87}Sr/^{86}Sr$ ratios and $\delta^{18}O$ values in the younger superunits (Cortecci et al. 1979; Del Moro et al. 1983a). Detailed summaries of research on the Adamello batholith are presented in Bianchi et al. (1970), Brack (1983), Callegari (1983), and Callegari and Brack (2002).

Re di Castello (sampling area 1) is the best studied of the four superunits. The emplacement age is ca. 42.4 to 40.9 Ma, yielding an intrusion span of ca. 1.5 Myr (Schaltegger et al. 2009). This superunit comprises the largest proportion of mafic material (see Fig. 1). Incremental growth with repose times long enough for sharp contacts to develop between some batches (Schaltegger et al. 2009; Brack 1983) is evident particularly in the southern part. In this contribution, we focused on the magma batches "Avortici," "Spotty Dog," and "Vacca" from the Lago della Vacca complex (Fig. 1b; as defined in John and Blundy 1993). For simplification, these three batches together are referred to as "LdV" in the following. Sharp contacts in the Lago della Vacca complex exist between "Blumone," "Vacca," and "Galliner Granodiorite" (Fig. 1b; as defined, e.g., in Ulmer et al. 1983). Between "Spotty dog" (SD) and "Avortici" (AV) (Fig. 1b), for example, discernible magma batches show diffuse, curvy contacts, and mingling. Heterogeneities in the studied batches comprise, for example, thin, leucocratic bands depleted in dark minerals, deformed mafic enclaves (Fig. 2a), and xenoliths. The development of a pronounced planar fabric within these batches likely occurred synchronously with magma intrusion (John and Blundy 1993). The samples studied in more detail (Ada14-AVx) are from "Avortici."

Western Adamello Tonalite (WAT, sampling area 2) is one of the two discernible batches of the Adamello superunit, and was emplaced within ca. 1.2 Myr, from ca. 37.6 to 36.4 Ma (Floess and Baumgartner 2015). In contrast to LdV, WAT is mainly composed of largely homogeneous tonalite and possesses only minor amounts of gabbro, along its border (Callegari 1983). It appears heterogeneous on a decimeter- to meter-scale. For example, WAT exhibits: (1) biotite-hornblende-dominated crystal clots of up to a few millimeters in diameter, (2) abundant fine-grained dioritic to gabbroic enclaves, which most likely originate from dikes that were injected into and mingled with the crystal mush, (3) some pieces of mafic cumulate, (4) rare xenoliths of crustal origin, and (5) leucocratic bands (centimeter to decimeter thick) that are variably depleted in biotite and hornblende and show diffuse to sharp transitions into their host tonalite (Fig. 2b). Pervasive foliation is characteristic for the southern "External Zone" of WAT, which was interpreted as a conduit that transported magma upward (Floess and Baumgartner 2015), but is rare in sampling area 2, which is part of the "Internal Zone" (Floess and Baumgartner 2015). The samples studied in more detail (Ada14-AFx) are derived from the "Internal Zone" of WAT.

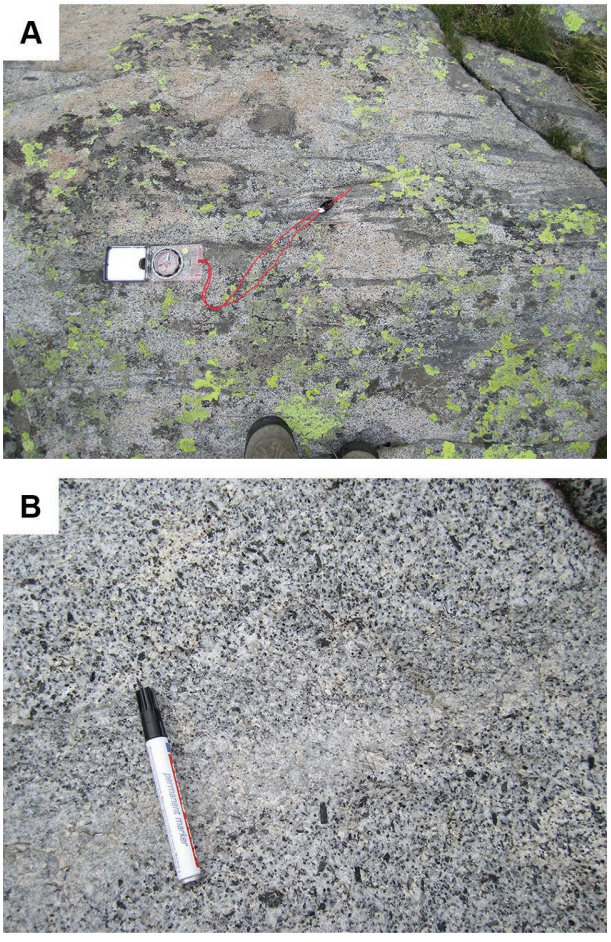

FIGURE 2. Field observations. (**a**) Flattened mafic enclaves in foliated Re di Castello quartz diorite. (**b**) Leucocratic segregation band, exhibiting variable thickness and lack of amphibole and biotite in Western Adamello tonalite. The transition from leucocratic band to homogeneous tonalite is not sharp. The homogeneous tonalite contains randomly oriented, large hornblende crystals, and clots of dark minerals or mafic enclaves. (Color online.)

METHODOLOGY

Bulk-rock and mineral chemistry

Major element compositions of the bulk-rock were determined by X-ray fluorescence (XRF) spectroscopy on fused glass beads, with a PANalytical Axios XRF spectrometer at the Department of Earth Sciences, ETH Zurich. An accelera-

tion voltage of 24–60 kV and a current of 40–100 mA were applied. Calibration was carried out on 35 internationally accepted standard powders processed to glass beads. The limit of detection is <0.012 wt% for all oxides.

Major element compositions of all major phases in four samples (Ada14-AV1a, -AV2, -AF14, and -AF15) were determined for mass-balance calculations (aimed at the crystallized liquid fraction). They were measured with a JEOL JXA-8200 electron probe microanalyzer (EPMA) at the Department of Earth Sciences, ETH Zurich. An acceleration voltage of 15 kV and a beam current of 20 nA were applied, with a spot size of 1–5 μm. Natural and synthetic silicates and oxides were used as standards. Samples were carbon coated (ca. 20 nm thickness). Backscatter electron images were used in combination with major element profiles across plagioclase and hornblende to distinguish between different zones.

Trace element compositions of the bulk-rock and all major mineral phases were determined with laser ablation-inductively coupled plasma-mass spectrometry (LA-ICP-MS) at the Department of Earth Sciences, ETH Zurich. For the bulk-rock, an Elan 6100 DRC (Perkin Elmer, Canada) mass spectrometer, coupled to a 193 nm ArF Excimer GeoLas (Coherent, Germany) system, was used. Glass beads (of the bulk-rock) were ablated with 90 μm spot size, 10 Hz repetition rate, and laser energy density of ca. 12 J/cm^2. Carrier gas flux was 1.1 L/min He, and auxiliary/sample gas flows were both ca. 0.8 L/min Ar. NIST SRM 610 served as external standard, ablated with 40 μm spot size and an energy density of ca. 5–7 J/cm^2. Calcium oxide contents (in wt%) from XRF analysis of the bulk-rock served as internal standard. A blank correction was carried out using a blank Li-meta-/tetraborate glass bead. The data from three measurements on each glass bead were averaged to get the bulk-rock concentrations.

Trace element analysis was conducted for mass-balance calculations. For all major mineral phases except quartz, a Thermo-Element XR mass spectrometer connected to a 193 nm Resonetics ArF Excimer laser was used. The laser was operated in a double-volume Laurin Technic S155 ablation cell with a spot size of 19 μm, a repetition rate of 5 Hz and a laser energy density of ca. 3.5 J/cm^2. Carrier gas flow was 0.7 L/min He, and auxiliary/sample gas flows were both ca. 1.0 L/min Ar. Major element data from EPMA were used as internal standards, NIST SRM610 for external standardization and GSD-1G basalt glass as a secondary standard. Trace elements in quartz were measured with the same instrument and setup as for bulk-rock trace elements, except that the laser energy density was higher (ca. 13–16 J/cm^2), and SiO_2 content (set as 99.9 wt%) was used as internal standard. The MATLAB-based software SILLS (Guillong et al. 2008) was used for data reduction, including time-dependent instrumental drift, gas blank, and relative sensitivity corrections, for the bulk-rock and all major phases.

Cathodoluminescence imaging

Cathodoluminescence (CL) images were obtained on an ERI-MRTech optical CL microscope with a cold cathode mounted on an Olympus BX41 petrographic microscope at the University of Geneva. Acquisition conditions were: gun current of ca. 300 μA, high voltage of ca. 11 kV, defocused beam with a diameter of ca. 1 cm, residual pressure of ca. 50 mTorr. Samples were uncoated and the chamber was flushed with Ar.

Phase and plagioclase maps

Energy-dispersive X-ray spectroscopy (EDS) scanning was applied to obtain compositional maps of thin sections. For EDS scans and spot analyses, thin sections were coated with a ca. 20 nm thick carbon layer. Ten EDS maps were produced using a Jeol JSM-6390LA instrument at the Department of Earth Sciences, ETH Zurich, equipped with a Thermo-Fisher Ultradry EDS detector coupled to a Thermo-Fisher Noran System 7 and an LaB_6 filament or a tungsten filament. An acceleration voltage of 15 kV was applied. Scanning mode was 10 frames for 60 s each with 22 700 counts per second, and a resolution of 128 × 96 pixels, resulting in a step size of ca. 20 μm.

Phase maps and plagioclase maps (plagioclase was selected because of its variable composition and broad crystallization interval) were created with the PARC-based spectral image processing software iSpectra (Liebske 2015), written in WaveMetrics' Igor Pro. Area% was directly converted to volume%, i.e., these were assumed to be equal.

An error of up to a few percent for most phases is introduced by direct conversion from area% to volume%, as a comparison between the results from phase maps and CIPW norm (Kesley 1965; Cox et al. 1979) revealed. This is acceptable for at least the major phases quartz, plagioclase, alkali feldspar, and probably hornblende. It may, however, introduce a larger error for platy minerals such as biotite in foliated samples. Reliability of the estimates of the phase proportions can be improved through scans over a larger area, which is particularly important for coarse-grained samples, and on variably oriented sections through the sample. The stereological basics for conversion were discussed, for example, by Sahagian and Proussevitch (1998), Higgins (2000 and references therein), and Jerram and Higgins (2007). The quantification of anorthite contents by EDS is affected by an error of up to a few percent, with a tendency to produce slightly overestimated anorthite contents (the calibration curve that relates Si/Al intensity ratios with anorthite contents in plagioclase was acquired with slightly different settings for better spectral resolution than the plagioclase maps themselves).

Electron backscatter diffraction

Electron backscatter diffraction (EBSD) measurements on entire thin sections were conducted using a TESCAN VEGA 3 XLH scanning electron microscope at the Department of Materials, ETH Zurich. Analysis settings were: sample tilt of 70°, acceleration voltage of 20 kV, high vacuum, working distance of ca. 35 mm. Small-scale EBSD measurements on individual plagioclase crystals were conducted using an FEI Quanta 200 FEG scanning electron microscope at the Electron Microscopy Center, ETH Zurich. Analytical settings were as follows: sample tilt of 70°, acceleration voltage of 20 kV, low vacuum of 30 Pa, and working distance of ca. 17 mm. Intracrystalline deformation (bending) of plagioclase was studied through misorientation angles, in two different samples, the foliated sample Ada14-AV1a from LdV and the unfoliated sample Ada14-AF15 from WAT. The error of the EBSD method is often specified to be at least 1° for silicate minerals due to technical limitations (software manual; Prior et al. 1999; Schwartz et al. 2009).

The program OIM data collection by Ametek-EDAX was used to acquire EBSD patterns, with a pixel binning of 4 × 4. Step size was 40 μm for large-scale and 10 μm for small-scale scans. The EBSD measurements were coupled to EDS measurements for better phase assignment and thus more reliable indexing (software option ChiScan). The program OIM Analysis was used to process the collected data. Indexing files for albite, hornblende, quartz, and orthoclase were used. Filtering for the different phases was based on compositional criteria and adjusted with the software's built-in functions (confidence index and grain size). Grains smaller than 10 pixels were removed; filtering for larger grain sizes (e.g., >300 pixels) and vice versa does not cause any significant change to the CPO (not presented here).

The Matlab toolbox Mtex (Hielscher and Schaeben 2008; Bachmann et al. 2010) was used to process and analyze the cleaned and filtered EBSD data. Calculation of orientation distribution functions (ODF, Bunge 1982) and quantification of CPO was based on the eigenvalue (Vollmer 1990; Mauler et al. 2001; Mainprice et al. 2014). In the following, this approach is termed "Point-Girdle-Random (PGR)" method.

Errors in the CPO quantification can be introduced by: (1) variable indexing reliability due to different crystal orientations and (2) variable composition of the mineral phase. The effect of the plagioclase composition on the indexing, however, is assumed to be minor (Lapworth et al. 2002; Schwartz et al. 2009, their Fig. 26.7).

Bulk-rock trace element compositions

The two units from Re di Castello displayed in Figure 3 feature trends with significant scatter over a wide range of trace element concentrations. Not only the data for the Re di Castello superunit as a whole (red field) but also for separate units (Val Fredda: red triangles; this unit was selected because of its wide coverage in terms of bulk-rock data in the literature) show significant trace element scatter. The samples studied in more detail also show significant differences in SiO_2 and trace element contents (Fig. 3). For a detailed discussion of major element trends see Macera et al. (1983).

The magnitude of data scatter may not originate exclusively from open-system processes. We propose that data scatter is enhanced by variable cumulate signatures in the analyzed rock samples (see also Walker et al. 2015; Lee and Morton 2015, for similar interpretations on different plutons), especially where elements change their bulk partition coefficient.

Petrography

Texture

Textural differences between LdV and WAT were encountered in grain size, shape and lattice preferred orientation, and

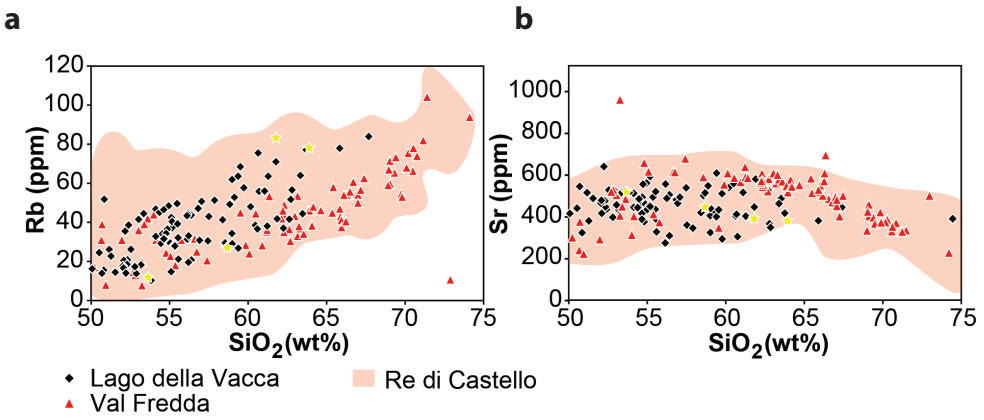

FIGURE 3. Diagram of (**a**) Rb vs. SiO_2 concentrations and (**b**) Sr vs. SiO_2 concentration from database (Macera et al. 1983; Blundy and Sparks 1992 and unpublished theses written at ETH Zurich. Data for the units Val Fredda (e.g., Broderick et al. 2015) and Lago della Vacca (including Blumone), are displayed as red and black symbols; data from the entire Re di Castello superunit (including enclaves, dikes, aplites, and pegmatites) are outlined by the red fields. Yellow stars represent compositions of samples Ada14-AV1a, -AV2, -AF14, -AF15—from left to right with increasing SiO_2 content. (Color online.)

intracrystalline deformation. Based on the lack of pervasive deformation textures at the scale of the superunits, post-emplacement subsolidus deformation in LdV and WAT is considered weak to absent. Therefore, the features described below relate exclusively to suprasolidus deformation, and, therefore, their relationship to the process of crystal-melt segregation can be examined in detail.

Samples from LdV are readily distinguished from those of WAT based on grain size and macroscopic textures. In LdV, grain sizes range between ca. 0.2–4 mm, with the smallest grain sizes encountered in "Avortici" and largest in "Spotty Dog." Crystal preferred orientation is present, forming a foliation but no pronounced lineation (first described by John and Blundy 1993). The intensity of foliations is variable within the studied (sub-)batches. In particular, plagioclase and hornblende crystals are aligned, leaving little pore space that is now filled by biotite, quartz (Figs. 4a and 5), alkali feldspar, and late-stage plagioclase (rim). Plagioclase clusters commonly consist of 2–10 crystals, some of which may share narrow, low-anorthite rims. Monomineralic clusters of hornblende and titanite commonly only consist of 2–3 crystals. Samples from "Avortici" and "Spotty Dog" are mostly strongly foliated, whereas the foliation in samples from "Vacca" is weaker. Both plagioclase (Fig. 6) and biotite may be bent. Hornblende twins are only rarely bent. Alkali feldspar may show deformation lamellae. Quartz usually shows undulose extinction.

Tonalite samples from WAT are significantly coarser grained (ca. 0.5–10 mm), and foliation is absent or subtle. Minerals in WAT are more heterogeneously distributed (e.g., plagioclase crystals may form chain-like networks). Plagioclase clusters occur randomly oriented in chains and as inclusions in large quartz oikocrysts. Clusters in WAT consist of fewer crystals compared to LdV. Large masses of quartz that appear to be individual grains are sometimes actually clusters of several grains, as CL images revealed. Quartz may show some undulose extinction, but evidence for intracrystalline deformation in other minerals is rare.

Mineralogy

The main minerals in the rock samples, all of which are quartz-diorites to tonalities, are: plagioclase (green in CL: Fig. 4), hornblende (non-luminescent, black in CL), quartz (dark blue in CL), and biotite (non-luminescent, black or dark green in CL, if chloritized). Alkali feldspar (turquoise in CL) can only be observed under the microscope. Color indices range from ca. 30 to 40. Samples from LdV are typically more mafic (quartz diorite) compared to those from WAT (tonalite), as they contain more hornblende and plagioclase, and less quartz and alkali feldspar [see section "Comparison of foliated (LdV) and unfoliated (WAT) samples" and Table 1 for mineral proportions].

Grain shape and mineral inclusions reveal the following crystallization sequence: (pyroxene) > hornblende+plagioclase > biotite+quartz > alkali feldspar, with most minerals crystallizing simultaneously over part of their crystallization interval. This crystallization sequence is supported by experimental work (Nandedkar 2014; Nandedkar et al. 2014). It is clearest for LdV but assumed to also apply to WAT.

Hornblende is relatively large (ca. 3 mm in Avortici to ca. 10 mm in WAT), euhedral to subhedral, and hosts randomly oriented plagioclase inclusions (John and Blundy 1993), apatite (yellow in CL), opaque minerals, and biotite flakes (the latter likely being near-solidus reaction products). Moreover, hornblende in LdV exhibits color zoning from a brown core to green rim (visible in transmitted light mode). In WAT, however, brown hornblende appears to be absent (or much rarer).

Plagioclase is euhedral to subhedral, the most abundant mineral in all studied samples, and can have inclusions of hornblende and opaque minerals. Its morphology is tabular (in LdV) to stubby columnar (in WAT). It forms a mostly equigranular texture with a few exceptionally large (>1 cm) crystals. Albite, Carlsbad, and Pericline twinning is frequent. Zoning can be summarized as follows (Supplemental[1] Data File 1): (1) cracked, inner core of $>An_{80}$, (2) outer core, characterized by pronounced oscillatory zoning between ca. $An_{75–45}$ and less

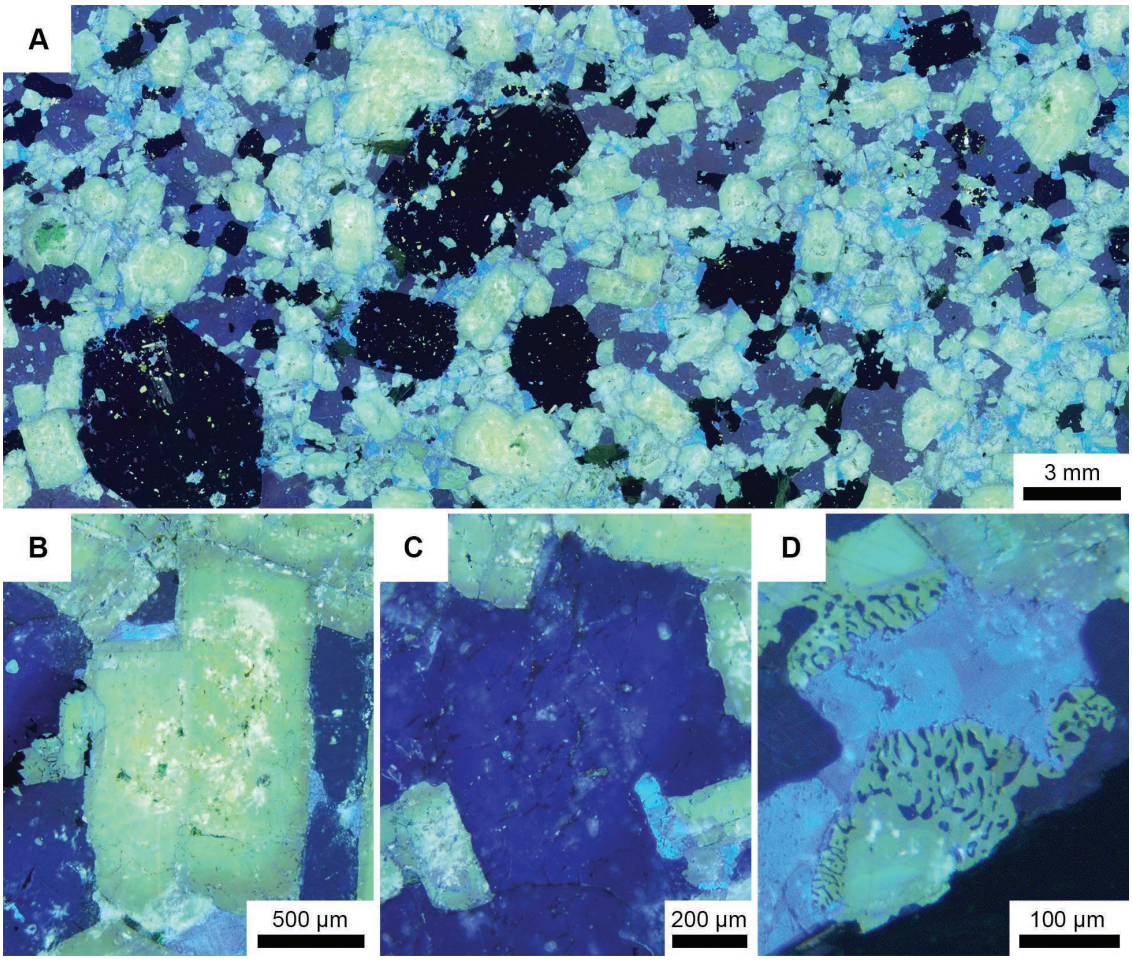

FIGURE 4. Optical cathodoluminescence images of samples from WAT (**a** and **d**) and LdV (**b** and **c**). Green = plagioclase, black = amphibole, biotite, dark blue = quartz, turquoise = alkali feldspar, yellow = apatite, dark green = chloritized biotite. (**a**) Overview image showing phase relations; (**b**) plagioclase cluster with dark green rim; (**c**) quartz with variable luminescence brightness; (**d**) myrmekite between zoned plagioclase and alkali feldspar. (Color online.)

or no oscillatory zoning between ca. $An_{50–40}$, and (3) normally zoned rim of $\leq An_{40}$ (Fig. 4b, light green to brown-green in CL, Fig. 5; Supplemental[1] Data File 1), in textural equilibrium with green hornblende rim, quartz, and biotite. The common brown-green rims (in CL) of plagioclase (Fig. 4b) likely correspond to low-anorthite rims quantified with phase maps (see below). Partly altered and fractured, inner cores are common in LdV (Figs. 4a, bright green in CL, 5) and rare or absent in WAT. Apart from high-anorthite inner cores, EPMA core-rim profiles show similar patterns (Supplemental[1] Data File 1) in samples from LdV and WAT.

Biotite and quartz crystals are larger and more abundant in WAT and "Vacca" than in "Avortici" and "Spotty Dog" [see section "Comparison of foliated (LdV) and unfoliated (WAT) samples," Table 1]. Biotite and quartz are anhedral in "Avortici" and "Spotty Dog" and anhedral to subheral in WAT and "Vacca." Biotite may be partly chloritized (Fig. 4a, dark green in CL).

Quartz reveals a mostly homogeneous color in CL (Fig. 4a), which can be attributed to generally low luminescence of quartz that prevents high contrast in cold-cathode CL and/or crystallization without significant variation in luminescence centers (i.e., trace element concentrations). There are rare exceptions of indicated brighter, inner parts of quartz in WAT (Fig. 4c). To a large part, however, brightness variations can be attributed to preparation artifacts, underlying non-luminescent minerals, and inclusion trails. Quartz and plagioclase forming myrmekite is common both in LdV and WAT at the interface between plagioclase and alkali feldspar (Fig. 4d). The CL color of myrmekite is indistinguishable of that in other plagioclase and quartz.

In such medium-K, calc-alkaline intermediate-to-silicic magmas, alkali feldspar should be the last phase to crystallize (e.g., Tuttle and Bowen 1958). Its anhedral shape as a result of crystallization within the interstices of other minerals (Fig. 4a) is evidence of that late growth. Alkali feldspar commonly reveals some color zoning with brighter, euhedral inner parts in CL (Fig. 4d).

[1]Deposit item AM-17-126026, Supplemental Material. Deposit items are free to all readers and found on the MSA web site, via the specific issue's Table of Contents (go to http://www.minsocam.org/MSA/AmMin/TOC/2017/Dec2017_data/Dec2017_data.html).

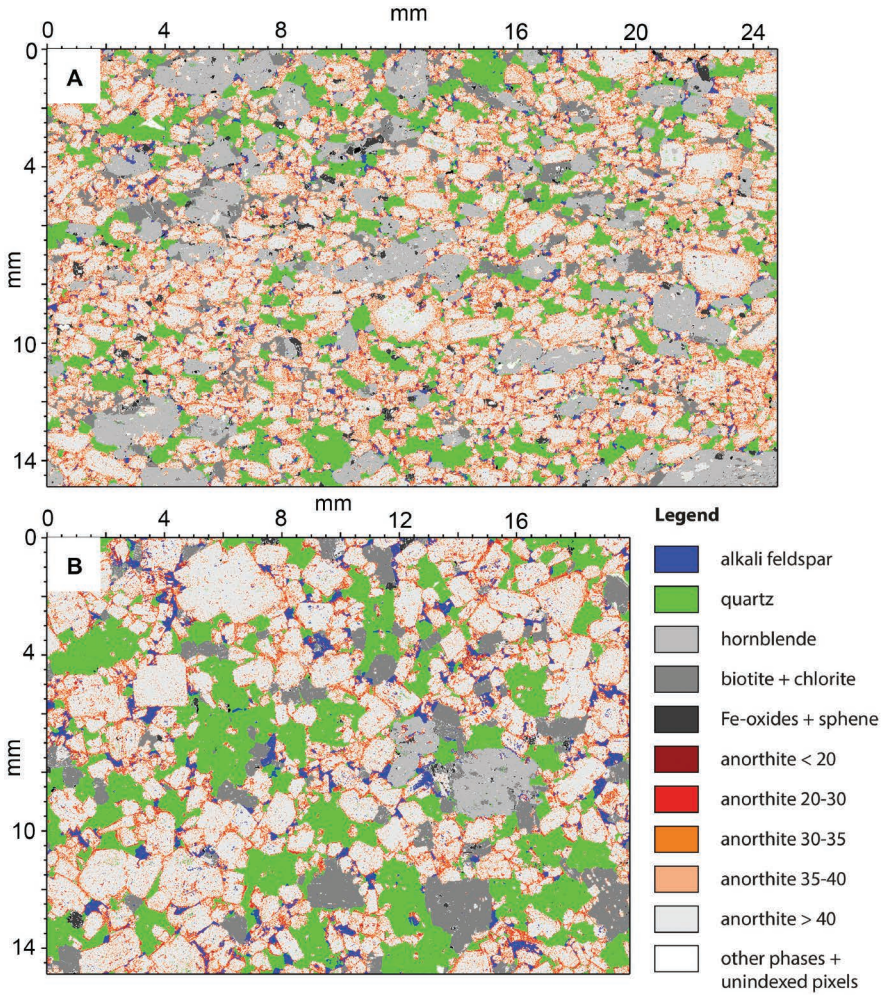

FIGURE 5. Combined phase and plagioclase maps based on SEM-EDS element mapping for (**a**) sample Ada14-AV2 from LdV, section perpendicular to foliation, and (**b**) for sample Ada14-AF14 from WAT. Colors correspond to different phases and anorthite contents. (Color online.)

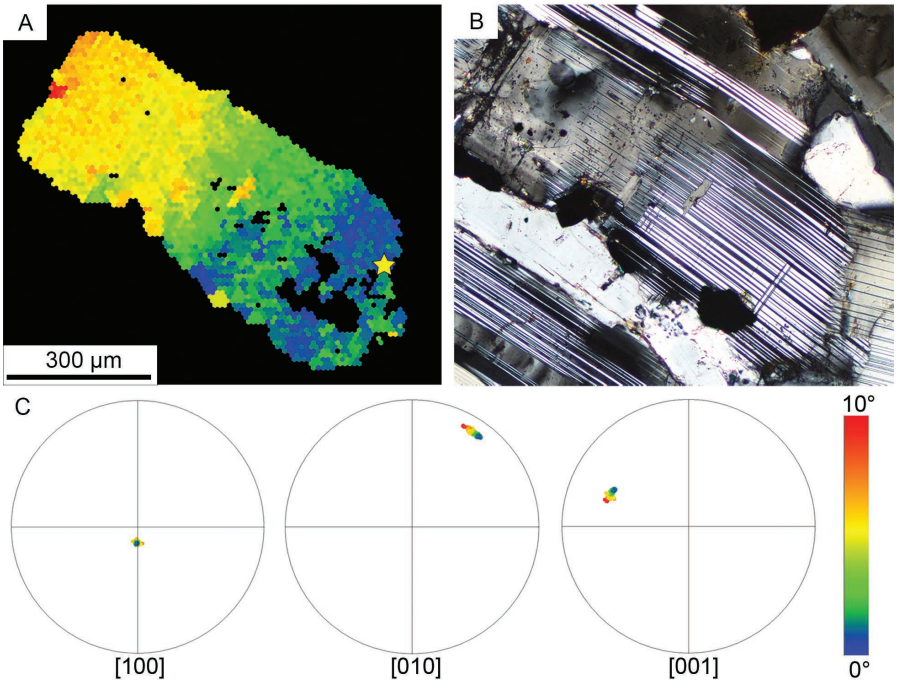

FIGURE 6. Bent plagioclase crystal of sample Ada14-AV1a from LdV. (**a**) Misorientation map: color coding corresponds to misorientation angle with respect to reference point (star), and reveals significant intracrystalline deformation. (**b**) Polarized light microscopic image: bending of the crystal is reflected in undulose extinction, lamellar deformation twins, and faint kinks. (**c**) Upper hemisphere, equal-angle stereographic projections of the three axes *a* [100], *b* [010], and *c* [001]. Rotation of the *b*- and *c*-axes about the *a*-axis is visible. (Color online.)

Table 1. Phase proportions (in area% or vol%, see text) as determined from EDS scans

	Qz	Afs	Pl[a]	Pl[b]	Hbl	Bt+Chl	FeOx+Ttn	Unind.
AV1a	7	2	20	41	23	1	2	4
AV2.i	15	2	23	36	14	6	1	3
AV2.ii	14	2	22	32	21	6	1	3
AV2.iii	12	2	22	37	17	5	2	3
SD2	11	2	21	38	17	7	2	3
VA3	23	2	12	39	5	14	1	5
AF14.1	22	5	17	37	5	12	0	3
AF15.1	29	6	16	24	11	12	1	2
AF16a3	35	7	26	27	0	3	0	2

Notes: Samples in rows 1–6 from LdV, in rows 7–9 from WAT. [a] Pl = plagioclase with $\leq An_{40}$; [b] Pl = plagioclase with $>An_{40}$; Unind. = unindexed pixels and accessory phases. The results for Ada14-AF14.1 are averaged from two thin section scans.

Several other minor phases appear in the samples:

- Patches of clinopyroxene in hornblende and irregular hornblende clots likely represent relicts of early crystallized clinopyroxene.
- Apatite is typically an early phase, as it is commonly included in early crystallizing minerals such as hornblende (Fig. 4a).
- Zircon appears to saturate at intermediate crystallinity, at ca. 60 wt% SiO_2 according to a changing trend in the Zr vs. SiO_2 diagram (not presented here; Supplemental[1] Data File 2).
- Epidote is also present in small quantities and is interpreted as secondary because its primary stability field does not reach pressures below ca. 5 kbar (NNO, H_2O-saturated; Schmidt and Thompson 1996).

Zoning forms in crystals as a result of disequilibrium, which can occur during: (1) simple fractional crystallization, (2) open-system behavior in the form of assimilation of preexisting rocks or magma recharge (Tiepolo et al. 2011), and/or (3) change in pressure-temperature conditions of the magma (e.g., Leuthold et al. 2014). Cracked inner cores of plagioclase, for example, may record an early crystallization history of LdV in a deeper, more mafic reservoir (see also Bachmann and Huber 2016: "polybaric mush model").

Determination of the amount of trapped liquid

Observations from phase and plagioclase maps of foliated (LdV) and non-foliated (WAT) samples

Samples from LdV and WAT exhibit clearly different mineral proportions (Fig. 5), calculated from EDS phase maps. Features associated with plagioclase (Table 1, columns 3–4), which is the dominant phase occurring over >40 area%, include the following:

- Overlapping, but, on average, lower total percentage of modal plagioclase (Table 1, columns 3–4) in WAT compared to LdV.
- Anorthite contents in plagioclase from WAT and LdV ranging between ca. $An_{90–20}$ with a plateau at $An_{60–40}$; common inherited, inner cores with high anorthite ($>An_{80}$) in LdV (Fig. 4).
- Overlapping percentages of low anorthite ($\leq An_{40}$) within plagioclase between LdV and WAT (Table 1, column 3; orange-red seams around grains in Fig. 5); exceptions are sample VA3 from "Vacca" (LdV), which contains only a low amount of plagioclase with $<An_{40}$ but larger amounts of biotite and quartz, and sample Ada14-AF16a3 from WAT.

Features associated with all other minerals include the following:

- Highly variable amounts of hornblende (Table 1, column 5), biotite+chlorite (Table 1, column 6), and quartz (Table 1, column 1), with rough correlation between amounts of quartz and [biotite+chlorite].
- Higher hornblende (Table 1, column 5) contents, on average, in LdV (except VA3) than in WAT (in particular, hornblende almost absent in Ada14-AF16a3).
- Significantly greater amounts of quartz and smaller amounts of biotite+chlorite in leucocratic part of one sample from WAT (AF16a3; Table 1, row 9).
- Always small amount of alkali feldspar (Table 1, column 2), and smaller in LdV in comparison to WAT.
- Small amounts of titanite+Fe-oxides (Table 1, column 7) in both cases; titanite tends to be more common in samples from LdV compared to WAT.
- Apatite and zircon present in small amounts in most phase maps but counted together with unindexed pixels (Table 1, column 8) because of uncertain percentages due to the coarse step size and small grain size.

Sample Ada14-AV2 from LdV was scanned in three orthogonal orientations to study anisotropy of melt segregation, i.e., of trapped liquid distribution, which is a common side-effect of the development of foliation (Hersum 2009). Orthogonal scans yield only small differences in the percentages of high-anorthite plagioclase and hornblende.

Minerals contributing to the trapped liquid

The trapped liquid is defined as the melt that crystallizes after the magma has reached the rheological lock-up (Vigneresse et al. 1996; Petford 2003; Dufek and Bachmann 2010). Hence, in an idealized system, if no melt extraction has occurred, the upper limit of the amount of trapped liquid should be ca. 50 vol%, ignoring ranges of lock-up crystallinity estimates for simplicity. Any values lower than this are, therefore, assumed to record melt loss i.e., crystal accumulation (in contrast to the crystallized liquid fraction, CLF, as calculated in Meurer and Boudreau 1998a, where 100% correspond to crystallization without loss of melt). The amount and composition of minerals growing after 50 vol% crystallization can be estimated using a presumed crystallization sequence based on existing experimental data under similar conditions on similar bulk-rock compositions (see, for example, classic study by Piwinskii 1973, but also Piwinskii and Wyllie 1968; Martel et al. 1999; Scaillet and Evans 1999; Costa et al. 2004; Cadoux et al. 2014; Nandedkar et al. 2014).

In the Adamello system, phases that crystallized most likely near the solidus are alkali feldspar, as well as quartz and biotite (although quartz and biotite could have small, likely re-equilibrated primocrystic cores). In contrast, plagioclase and hornblende are high-temperature phases, but capable of growing over a large crystallization interval (Nandedkar et al. 2014), hence having evolved rims that contribute to the trapped liquid. All other phases, including Fe-oxide, titanite, and apatite, are present in amounts <2% altogether and likely crystallized early, thus not adding much to the trapped liquid.

TABLE 2. Estimates for the amounts of "minimum" and "maximum trapped liquid," based on phase and plagioclase maps

	Minimum trapped liquid	Maximum trapped liquid
AV1a	7	31
AV2.i	15	46
AV2.ii	14	44
AV2.iii	12	41
SD2	11	41
VA3	23	50
AF14.1	22	55
AF15.1	29	62
AF16a3	35	71

Note: Samples in rows 1–6 from LdV, and in rows 7–9 from WAT.

A "maximum trapped liquid" (Table 2, column 1) was calculated specifically for the Adamello rocks, based on the above constraints. Here, we decided to include all alkali feldspar and quartz, plagioclase with $\leq An_{40}$ (rim), 90% of the biotite+chlorite (as some may have formed from amphibole), and 5% of the hornblende (approximate percentage of green rim before partial re-equilibration) in the "maximum trapped liquid." The results are:

- In samples from LdV, the "maximum trapped liquid" amounts to 31–50%. A "maximum trapped liquid" of 31% would correspond to a loss of ca. 27% melt from the parental magma, as no melt loss is assumed to result in 50% interstitial liquid and complete melt loss with opening of the extraction window at ca. 50% in 0% interstitial liquid.
- In samples from WAT, the "maximum trapped liquid" is ca. 55–62%. In the leucocratic part of sample Ada14-AF16a from WAT, it is ca. 71%.

In the case of the medium-K Adamello, a "minimum trapped liquid" (Table 2, column 2) can be calculated based on the eutectic phase assemblage that comprises ca. 1:1:1 of alkali feldspar:quartz:plagioclase (derived from Johannes and Holtz 1996; Johannes 1984; Ehlers 1972), assuming that all alkali feldspar is interstitial and crystallized last. Hence, as much quartz and plagioclase as alkali feldspar are assumed to be part of the "minimum trapped liquid" (resulting in plagioclase with an anorthite content of mostly $<An_{30}$). As MgO and FeO contents are commonly low in near-solidus silicic melts, mafic minerals (e.g., amphiboles) should play only a minor role for late-stage crystallization. Therefore, hornblende and biotite were not included in this "minimum trapped liquid." Using this technique, we find that the "minimum trapped liquid" estimates do not overlap for LdV and WAT.

- In samples from LdV, the "minimum trapped liquid" amounts to 6–7%.
- In samples from WAT, the "minimum trapped liquid" is at least 12–18%. In the leucocratic part of sample Ada14-AF16a from WAT, it is at least 20%.

The correlation between "minimum" and "maximum trapped liquid" estimates is positive and nearly linear (Table 2), which indicates that crystal-melt separation occurred predominantly within the main extraction window.

Quantification of the crystallized liquid fraction with geochemical modeling

Bulk-rock and average major and trace element compositions of the main mineral phases were used together to quantify modal abundances by mass balance (see Supplemental[1] Data File 3). Plagioclase inner and outer cores and brown hornblende cores were considered as early crystals, while plagioclase rims, hornblende green rims, quartz, zircon, titanite, magnetite, ilmenite, alkali feldspar, and biotite likely crystallized from the interstitial liquid. Despite its secondary origin, epidote was also considered in the mass-balance calculation to match bulk-rock geochemical analyses. Plagioclase-melt partition coefficients for Ba and Sr from Blundy and Shimizu (1991) were used to calculate the composition of the parental magma in equilibrium with plagioclase cores and rims. The chemistry of the parental liquids is assumed to be similar to the Re di Castello basaltic andesitic and andesitic dikes of Hürlimann et al. (2016), which also host: (1) high-anorthite plagioclase inner cores, and (2) overgrowth of plagioclase with anorthite content similar to that of the outer core determined in the plagioclase of this study (Hürlimann et al. 2016).

The CLF for K and Rb (CLF-K, CLF-Rb; Supplemental[1] Data File 3) was calculated with the method of Meurer and Boudreau (1998a). K_2O and Rb are incompatible elements along most of the Adamello liquid line of descent (Fig. 3). The Re di Castello basaltic andesitic and andesitic dikes of Hürlimann et al. (2016) that have appropriate Ba and Sr concentrations to match plagioclase core compositions (i.e., ca. 190 < Ba < 450 ppm, 180 < Sr < 600 ppm), contain 0.7–1.23 wt% K_2O and 15–43 mg/g Rb. Using the above conditions, sample Ada14-AV1a has a CLF-K of 0.39–0.60 and a CLF-Rb of 0.32–0.58. Using the same parameters, sample Ada14-AV2 has a CLF-K of 0.70–1.08 and a CLF-Rb of 0.86–1.53.

Samples from WAT are more differentiated than those from LdV, with higher K and Rb concentrations. In contrast to LdV, there is no indication of dikes cross-cutting the WAT. We thus tentatively consider bulk-rock compositions. For samples Ada14-AF14 and Ada14-AF15 from WAT, parental melts of intermediate compositions and with higher K and Rb contents (2.1 wt% K_2O and 90 mg/g Rb) were selected. The CLF-K and CLF-Rb calculations yield 0.85–0.91 and 0.86–0.91, respectively.

TEXTURAL INDICATORS FOR LOSS OF MELT

Quantification of the crystal preferred orientation

In samples from "Avortici" and "Spotty Dog" from LdV, strong CPO of plagioclase was observed (Fig. 7a). The long-axis of crystals in the 2D image are largely subparallel to the long edge of the thin section, and almost all plagioclase crystals in the thin section are connected. Pole figures (Fig. 7a) confirm this pronounced foliation: *b*-axes are aligned perpendicular to the foliation plane visible in the hand specimen, while *a*- and *c*-axes are mostly scattered within the foliation plane, roughly perpendicular to the orientation maximum of the *b*-axes. These *a*- and *c*-axes show diffuse maxima along the girdles in the pole figures, which indicate a faint lineation. Textural classification based on plagioclase crystal distribution in the foliated sample Ada14-AV1a from LdV (conducted with CSDcorrections: Higgins 2000, 2002) by means of the "R ratio" (Jerram et al. 1996) yields a value of 1.25 (in the section perpendicular to the foliation), indicating ordered patterns (i.e., the distribution is approaching maximum spacing between each crystal; Clark and Evans 1954). The strong foliation in samples from "Spotty Dog" and "Avortici" (LdV) correlates with only small amounts of "minimum" and "maximum trapped liquid" (Fig. 8, Table 2). Sample Ada14-VA3, representing "Vacca"

from LdV, is an exception as its crystals are randomly oriented, but it has a smaller "minimum trapped liquid" than samples from WAT.

In contrast, orientation maps of samples from WAT show nearly uniform CPO of plagioclase (Fig. 7b). No correlation of orientation with grain sizes could be observed. Crystals in plagioclase chains are randomly oriented. Pole figures and ODFs of samples from WAT highlight the lack of preferred orientation (Fig. 7b). Those peaks in orientation distribution that emerge from the ODFs are not consistent between the three axes. The "R ratio" (as described above) for unfoliated sample Ada14-AF15 is 0.87, indicating mostly random distribution with some clustering. The sample from "Vacca" is intermediate in textural character between the other studied batches from LdV and WAT. In the case of samples from WAT, a weak to absent foliation corresponds to large amounts of "minimum" and "maximum trapped liquid" (Fig. 8, Table 2).

Intracrystalline deformation of plagioclase

Intracrystalline deformation was observed in some plagioclase crystals (ca. 5% with microscopically visible bending) from LdV (Fig. 6), predominantly along the long sections (perpendicular to the *b*-axis) of the grains, whereas samples from WAT did not show any intracrystalline deformation. The diameter of all analyzed crystals or twin domains was <1 mm (in LdV). Up to ca. 13° misorientation along the long section of the grain was measured, in a grain without indication of subgrain formation. However, grains with more than ca. 5° misorientation commonly already showed the beginning of the development of subgrains. Along the long section of the grains, rotation about different axes was observed. Misorientation angles across grains from LdV are larger than in those from Ada14-AF15 from WAT (close to 0°), even though the grain sizes in LdV are smaller.

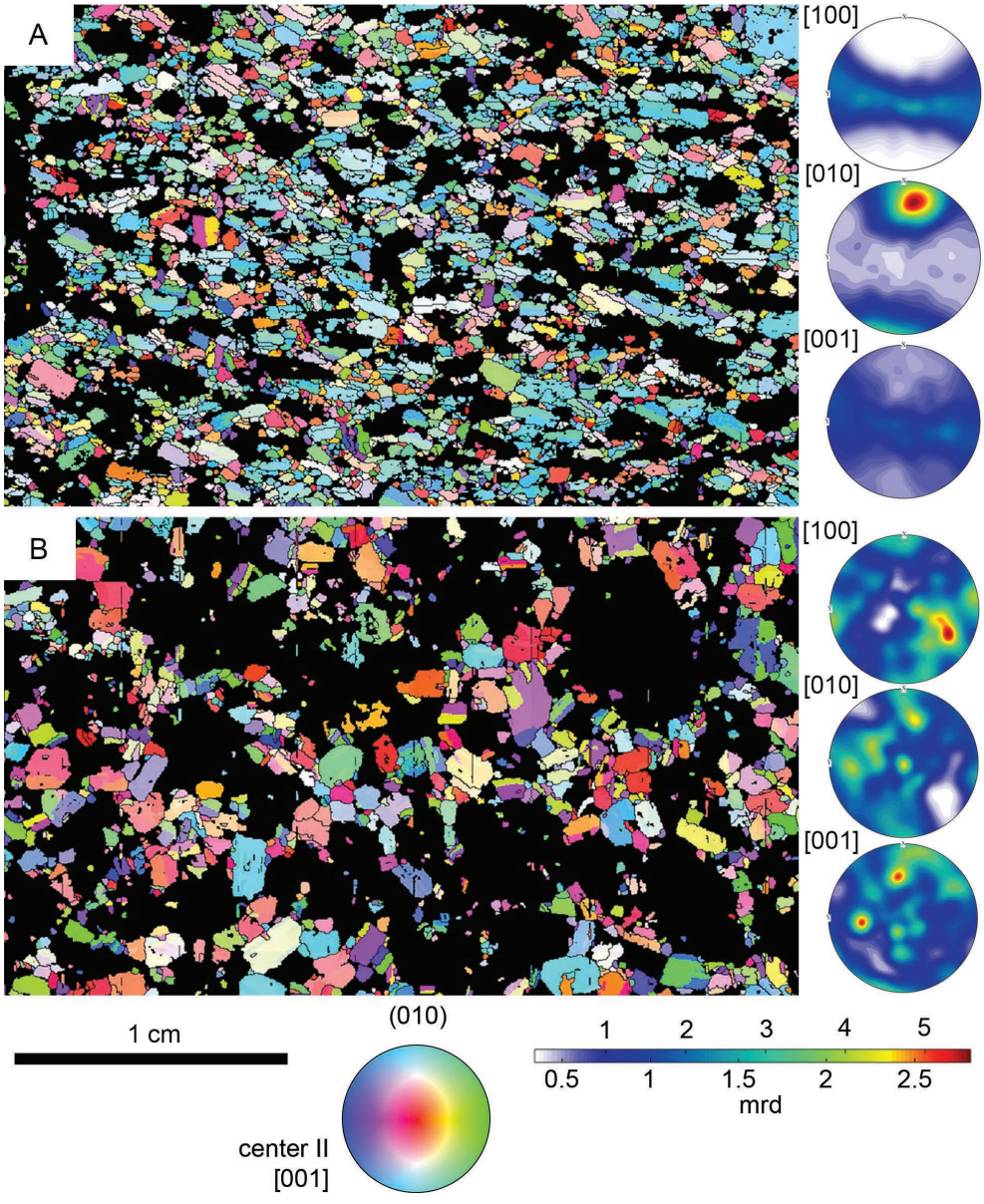

FIGURE 7. (**a**) Inverse pole figure-color coded crystal orientation map of strongly foliated sample Ada14-AV1a from LdV. Predominant turquoise color of the plagioclase crystals indicates preferred orientation of the *b*-axes parallel to the short edge of the scan (perpendicular to the visible foliation). The long edge of the thin section was oriented parallel to visible foliation. Twins were excluded before crystals were outlined. Only plagioclase is displayed in color, all other phases are black. Plagioclase crystal orientation depicted by the three pole figures for crystallographic axes *a* [100], *b* [010], and *c* [001], displayed in equal area density distributions calculated on the basis of a harmonic ODF with Mtex. Grains smaller than five pixels were removed. (**b**) Crystal orientation map of a sample that is rich in trapped liquid, Ada14-AF15 from WAT. No predominant color indicates lack of preferred alignment of crystals with respect to the thin section short edge. Three pole figures show random orientations. Scale above color bar corresponds to **a**, and scale below corresponds to **b**. (Color online.)

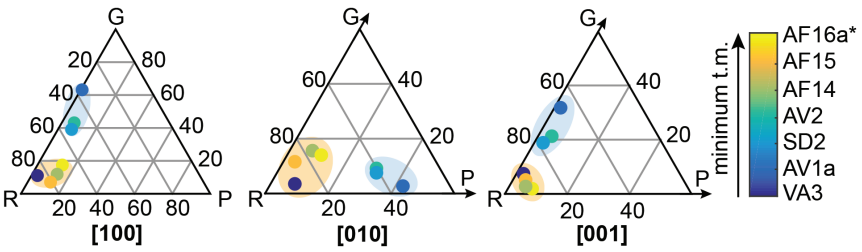

Figure 8. Quantification of CPO with the Point-Girdle-Random (PGR) method after Mainprice et al. (2014) and Vollmer (1990). The calculation was done for each crystallographic axis separately, resulting in three triangles. Samples at the blue end of the color bar have a smaller amount of "minimum trapped melt" (t.m.) then those at the yellow end. * The leucocratic part of this sample (Ada14-AF16) was analyzed. (Color online.)

Discussion

Significance of "minimum" and "maximum trapped liquid" estimates

The method presented here is aimed at estimating the amount of trapped liquid, and it targets both the melt separated in the main extraction window between ca. 50–70% crystallinity (e.g., Dufek and Bachmann 2010) and late-stage extraction (mostly by compaction) close to the solidus (Fig. 9). Very good correlation between "minimum" and "maximum trapped liquid" estimates, like in this study (Table 2), indicate that crystal-melt separation occurred predominantly within the main extraction window.

The "maximum trapped liquid" estimate strongly depends on the crystallization sequence and varies with mineral phases (including anorthite contents) that are allocated to the interstitial liquid. Different samples and magma batches are only comparable, if all followed the same (or very similar) crystallization sequence, starting with similar magma composition. Therefore, reliable results are expected when comparing samples of the same differentiation series. In addition, the selected crystallinity at which the main extraction window should open influences the interpretation. It should also be noted that there is clear evidence of compaction with intracrystalline deformation in LdV, indicating that some melt extraction must have occurred beyond the main melt extraction window (as defined in Dufek and Bachmann 2010).

The "minimum trapped liquid" is robust against minor variations of the crystallization sequence (and, hence, also of the parental magma composition), as it considers only the eutectic phase assemblage (Fig. 9, late stage). Thus, it can be useful where different parental magma compositions preclude meaningful estimates based on the "maximum trapped liquid." However, the "minimum trapped liquid" may vary not only with the extent of preceding melt extraction, but also with the selected proportions of the eutectic phase assemblage (and late percolation of K-enriched fluids). The selected eutectic composition is simplified and, in reality, depends on melt composition (particularly CaO, K_2O, H_2O content, and peraluminous vs. metaluminous melt composition), pressure, and temperature (in the Ab-An-Or diagram: von Platen 1965; Johannes and Holtz 1996).

Evidence of crystal accumulation based on the amount of trapped liquid

The rock samples from "Avortici" and "Spotty Dog" can be interpreted as cumulates that have formed by different degrees of crystal-melt segregation based on their relatively low amount of "minimum" and "maximum trapped liquid" in combination with strong foliation and intracrystalline deformation. In contrast, CPO and the amount of liquid extraction in WAT samples collected in this study may be small enough to term this magma batch a frozen melt body. The "minimum trapped liquid" in parts of LdV is lower than predicted by Lee and Morton (2015) (always ca. 20–30 vol% trapped in cumulates) and overlaps with the typical amount of intercumulus material in mafic to ultramafic mesocumulates (Irvine 1982). Such low amounts of trapped liquid are partly due to the fact that we do not take into account a large enough volume of rims around primocrysts (particularly plagioclase), but could also be due to some amount of compaction enhancing the melt extraction, as evidenced by intracrystalline deformation.

The leucocratic part (Fig. 2b) of one sample from WAT, Ada14-AF16a, contains significantly more "maximum trapped liquid" than all other samples. John and Stünitz (1997) suggested that such leucocratic bands were generated by shearing in a deforming crystal mush (see also Caricchi et al. 2007). However, a detailed analysis of such leucocratic bands is beyond the scope of this study.

The more mafic character of the studied LdV samples compared to WAT may partly be a result of greater melt loss, although it should be kept in mind that "Avortici" and "Spotty Dog" may have a more primitive parental magma composition than WAT and "Vacca." The former show less crustal contamination (Del Moro et al. 1983a; Cortecci et al. 1979; Bigazzi et al. 1986) than other batches and may, thus, have had lower initial K_2O and Rb concentration to start with, which in turn would lead to a larger calculated loss of trapped liquid than is actually the case.

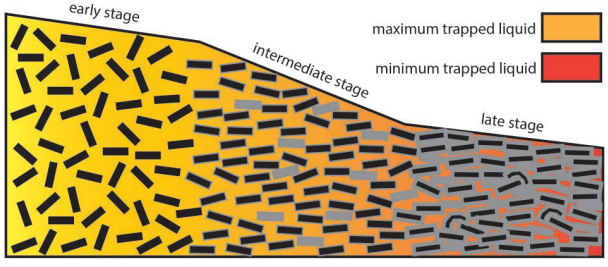

Figure 9. Melt extraction and development of CPO in the crystallizing magma chamber. Color variation indicates change of melt composition, and formation of new crystals and overgrowth rims (gray), by fractional crystallization. Volume decrease from early to late stage indicates melt extraction. Early stage: Free-floating crystals before the rheological lock-up. Intermediate stage (main melt extraction window): The rheological lock-up is reached, a foliation develops, and melt is lost. The remaining melt at this stage corresponds to the "maximum trapped liquid." Late stage: At high crystallinity, compaction supposedly dominates melt extraction and is indicated by crystal bending. The remaining interstitial melt at this stage corresponds to the "minimum trapped liquid." (Color online.)

Integration with bulk-rock trace element matching

Results from bulk-rock trace element matching are largely, but not perfectly, in agreement with the estimations of the interstitial liquid from phase maps and CPO, but also highlight the difficulties in identifying and quantifying the interstitial liquid or CLF in intermediate-to-silicic plutons:

- Considering any possible parental melt composition, CLF calculations for sample Ada14-AV1a always show melt loss: that is, about 32–60% of the rock consists of trapped crystallized melt (calculated CLF of ca. 0.32–0.60), and ca. 68–40% (1-CLF) are cumulus crystals. This is in agreement with strongly developed CPO and low estimates of "minimum" and "maximum trapped liquid."
- The calculated CLF for sample Ada14-AV2 is closer to 1, indicating little or no interstitial melt loss. This is in agreement with the lower abundance of cumulus crystals and higher abundance of biotite and quartz compared to sample Ada14-AV1a in phase maps. However, sample Ada14-AV2 is foliated and also contains high-anorthite inner cores of plagioclase.
- Estimates of the CLF for samples from WAT are close to 1, indicating a chemistry close to quenched liquid. This is compatible with the absence of foliation, the high modal abundance of quartz, alkali feldspar, and biotite, and the absence of distinct hornblende and plagioclase cores.

Calculation of the CLF largely depends on the choice of parental compositions, average trace element contents of minerals, and robust estimation of minerals contributing to the cumulus assemblage or interstitial liquid. Natural dikes in the Re di Castello and bulk rocks from WAT show large variations in trace element concentrations (Hürlimann et al. 2016; Macera et al. 1983). Consequently, the calculated range of CLF is wide, rendering estimates of melt loss less precise. Moreover, the CLF calculations yield slightly different values depending on the selected element. This also relates to differences in parental magma composition and variable mineral modes. Finally, estimation of the parental liquid chemistry from bulk-rock geochemistry of samples within the studied unit (not dikes), as for samples from WAT, is non-ideal because these may have already lost melt. It has to be kept in mind that, by definition, complete lack of melt loss should yield a CLF of 100% (Meurer and Boudreau 1998a) and a "maximum trapped liquid" of 50%.

Mechanisms generating magmatic foliation

Magmatic foliations and intracrystalline deformation of plagioclase are obvious in LdV. Both magmatic flow (near-liquidus) and submagmatic flow (near-solidus) (as defined by Paterson et al. 1989) can lead to such textures, assuming no significant subsolidus deformation due to tectonics has occurred. A magmatic mineral fabric was also observed by Turnbull et al. (2010, in the Halfmoon Pluton, New Zealand; see also references therein) and interpreted to have resulted from similar mechanisms as those discussed below.

Magmatic flow is an efficient mechanism to generate a fabric due to the higher mobility at relatively low crystallinity. It is featured by crystal rotation without plastic deformation (Paterson et al. 1989) and could be responsible for the orientation of early crystallized plagioclase and hornblende crystals, and schlieren structures. Magmatic flow may also include marginal upflow of compositionally relatively evolved melt along the magma chamber walls (Spera et al. 1995). This process, although largely rejected in more recent publications (e.g., Bachmann and Bergantz 2004), might generate vertical foliation, may lead to crystal-melt segregation, and is potentially most efficient where the magma chamber's sidewalls are steep and vertically extensive (de Silva and Wolff 1995; Spera et al. 1995). However, a pronounced lineation in addition to foliation is usually expected to develop in the course of magmatic flow (e.g., Brothers 1964; Wager and Brown 1968—for a large number of case studies; Meurer and Boudreau 1998b; Žák et al. 2008). Absence of lineations may be the result of limited flow of the magma or of overprinting by later processes. There are also some cases of magma flow without generation of lineation documented (Higgins 1991; Nicolas 1992).

Submagmatic flow, on the contrary, lacks suspension-like behavior but still takes place under suprasolidus conditions (Paterson et al. 1989). Mechanisms operating in this flow regime (Paterson et al. 1989; Meurer and Boudreau 1998b) that can generate planar fabrics are hindered settling and compaction (e.g., McKenzie 1984, 1985; Davis and Acrivos 1985; Bachmann and Bergantz 2004; Lee and Morton 2015). It is expected that all magmas go through a phase of hindered settling (indicated, for example, by crystal clusters; Graeter et al. 2015), and can then transition into a compaction stage, if viscosities are low enough and cooling rates slow enough. Some compaction has apparently occurred in LdV, as the observed deformation (bending, development of deformation twins, and kinking of crystals) implies. However, compaction is slow in shallow silicic systems (McKenzie 1985; Wickham 1987; Bachmann and Bergantz 2004; Lee and Morton 2015). Therefore, it should not generate strong foliation (e.g., Higgins 1991) and may not have generated much additional melt extraction.

Development of foliation and compaction features were likely reinforced by magma emplacement through ballooning (e.g., Holder 1979) in the case of LdV (John and Blundy 1993; Schoene et al. 2012). Strong evidence for forceful injection of magma batches before solidification of precursor batches was provided by John and Blundy (1993) on the basis of extensive strain measurements.

Implications

Understanding the volcanic-plutonic connection is one of the most prominent research topics in igneous petrology (Bachmann et al. 2007; Lipman 2007; Glazner et al. 2008; Annen 2009; Huber et al. 2012; Cashman and Sparks 2013; *Elements* issue from April 2016 on the "Enigmatic Relationship Between Silicic Volcanic and Plutonic Rocks"; Bachmann and Huber 2016; Cashman et al. 2017). Melt extraction from highly crystalline magma reservoirs (crystal mush) is key in understanding crustal differentiation and does not only contribute to geochemical diversity, but is also the logical first step in generating volcanic rocks from magma chambers.

Reliable evidence for crystal accumulation in plutonic lithologies includes magmatic foliation, crystal bending, and relatively low amounts of trapped liquid. The method presented in this paper is able to resolve variability in melt extraction within a pluton that was relatively homogeneous upon emplacement; estimation of volumes of melt extracted from mushy reservoirs is more robust,

if the parental melt composition and crystallization sequence are well known. If this is not the case, we argue that relative differences in crystal-melt segregation may still be resolvable through the abundance of the eutectic phase assemblage ("minimum trapped liquid" fraction; see Fig. 9 for conceptual model).

Assessment of the significance of the data presented here with respect to entire batholiths requires more systematic, dense sampling over a larger area of the plutons to study, e.g., how consistent the textures are on a larger scale and how robust the correlation between texture and trapped liquid is. Hence, further studies should look at the largest possible number of samples with variable texture strength from a coherent differentiation series. Moreover, a combination of different approaches, which provide different pieces of evidence for crystal-melt segregation, is key to assess the relative contributions of different mechanisms, such as hindered settling, compaction, and filter-pressing. For example, the correlation between CPO and amount of trapped liquid observed in our study may imply that deformation during crystallization of crystal mushes is an efficient way to extract interstitial liquid (e.g., by Caricchi et al. 2007).

Acknowledgments

This research was supported by SNF fund no. 200020_165501 to O. Bachmann. We thank Christian Liebske (extensive computational support with iSpectra), Lydia Zehnder, and Markus Wälle (XRF measurements and support at LA-ICP-MS, respectively, for samples analyzed in the course of this project). Thanks to Dina Klimentyeva for EPMA and LA-ICP-MS analyses of minerals. Access to SEM-EBSD systems at ETH Zurich (Laboratory for Nanometallurgy and ScopeM) is acknowledged. We also thank Felix Marxer and Maren Wanke for discussions and literature suggestions and Ben Ellis and Meredith Townsend for comments on an earlier version of this manuscript. J. Leuthold (responsible for CLF calculations) acknowledges support from a Swiss National Science Foundation (SNSF) Ambizione grant. Comments from J. Otamendi and an anonymous reviewer and editorial handling by C. Barnes are greatly appreciated.

References cited

Anderson, A.T.J., Swihart, G.H., Artioli, G., and Geiger, C.A. (1984) Segregation vesicles, gas filter-pressing, and igneous differentiation. The Journal of Geology, 55–72.

Annen, C. (2009) From plutons to magma chambers: Thermal constraints on the accumulation of eruptible silicic magma in the upper crust. Earth and Planetary Science Letters, 284, 409–416.

Bachmann, O., and Bergantz, G. (2004) On the origin of crystal-poor rhyolites: Extracted from batholithic crystal mushes. Journal of Petrology, 45, 1565–1582.

——— (2006) Gas percolation in upper-crustal silicic crystal mushes as a mechanism for upward heat advection and rejuvenation of near-solidus magma bodies. Journal of Volcanology and Geothermal Research, 149, 85–102.

——— (2008) The magma reservoirs that feed supereruptions. Elements, 4.1, 17–21.

Bachmann, O., and Huber, C. (2016) Silicic magma reservoirs in the Earth's crust. American Mineralogist, 101, 2377–2404.

Bachmann, O., Miller, C.F., and de Silva, S.L. (2007) The volcanic–plutonic connection as a stage for understanding crustal magmatism. Journal of Volcanology and Geothermal Research, 167, 1–23.

Bachmann, F., Hielscher, R., and Schaeben, H. (2010) Texture analysis with MTEX—Free and open source software toolbox. Solid State Phenomena, 160, 63–68.

Bacon, C.R., and Druitt, T.H. (1988) Compositional evolution of the zoned calcalkaline magma chamber of Mount Mazama, Crater Lake, Oregon. Contributions to Mineralogy and Petrology, 98, 224–256.

Barnes, C.G., Coint, N., and Yoshinobu, A. (2016) Crystal accumulation in a tilted arc batholith. American Mineralogist, 101, 1719–1734.

Bartley, J.M., Coleman, D.S., and Glazner, A.F. (2006) Incremental pluton emplacement by magmatic crack-seal. Earth and Environmental Science Transactions of the Royal Society of Edinburgh, 97, 383–396.

Beane, R., and Wiebe, R.A. (2012) Origin of quartz clusters in Vinalhaven granite and porphyry, coastal Maine. Contributions to Mineralogy and Petrology, 163, 1069–1082.

Bédard, J.H. (1994) A procedure for calculating the equilibrium distribution of trace elements among the minerals of cumulate rocks, and the concentration of trace elements in the coexisting liquids. Chemical Geology, 118, 143–153.

Ben Ismaïl, W., and Mainprice, D. (1998) An olivine fabric database: an overview of upper mantle fabrics and seismic anisotropy. Tectonophysics, 296, 145–157.

Bianchi, A., Callegari, E., and Jobstraibizer, P.G. (1970) I tipi petrografici fondamentali del Plutone dell'Adamello. Tonaliti, quarzodioriti, granodioriti e loro varietà leucocrate. Memorie dell'Istituto Geologico della R. Università di Padova, 27, 1–148.

Bigazzi, G., Del Moro, A., and Macera, P. (1986) A quantitative approach to trace element and Sr isotope evolution in the Adamello batholith (northern Italy). Contributions to Mineralogy and Petrology, 94, 46–53.

Blundy, J.D., and Shimizu, N. (1991) Trace element evidence for plagioclase recycling in calc-alkaline magmas. Earth and Planetary Science Letters, 102, 178–197.

Blundy, J.D., and Sparks, R.S.J. (1992) Petrogenesis of mafic inclusions in granitoids of the Adamello Massif, Italy. Journal of Petrology, 33, 1039–1104.

Blundy, J.D., and Wood, B. (2003) Partitioning of trace elements between crystals and melts. Earth and Planetary Science Letters, 210, 383–397.

Boyet, M., Lapierre, H., Tardy, M., Bosch, D., and Maury, R. (2001) Nature des sources des composants andesitiques des Gres du Champsaur et des Gres de Taveyannaz; implications dans l'evolution des Alpes occidentales au Paleogene. Bulletin de la Société Géologique de France, 172, 487–501.

Brack, P. (1983) Multiple intrusions—Examples from the Adamello batholith (Italy) and their significance on the mechanisms of intrusion. Memorie della Società Geologica Italiana, 26, 145–157.

Broderick, C., Wotzlaw, J.F., Frick, D.A., Gerdes, A., Ulianov, A., Günther, D., and Schaltegger, U. (2015) Linking the thermal evolution and emplacement history of an upper-crustal pluton to its lower-crustal roots using zircon geochronology and geochemistry (southern Adamello batholith, N. Italy). Contributions to Mineralogy and Petrology, 170, 1–17.

Brothers, R.N. (1964) Petrofabric analyses of rhum and skaergaard layered rocks. Journal of Petrology, 5, 255–274.

Bunge, H.-J. (1982) Texture Analysis in Materials Science: Mathematical Methods, 593 p. Butterworths, London.

Cadoux, A., Scaillet, B., Druitt, T.H., and Deloule, E. (2014) Magma storage conditions of large Plinian eruptions of Santorini Volcano (Greece). Journal of Petrology, 55, 1129–1171.

Callegari, E. (1983) Geological and petrological aspects of the magmatic activity at Adamello (Northern Italy). Memorie della Società Geologica Italiana, 26, 83–103.

Callegari, E., and Brack, P. (2002) Geological map of the Tertiary Adamello batholith (Northern Italy)—Explanatory notes and legend. Memorie di Scienze Geologiche, 54, 19–49.

Caricchi, L., Burlini, L., Ulmer, P., Gerya, T., Vassalli, M., and Papale, P. (2007) Non-Newtonian rheology of crystal-bearing magmas and implications for magma ascent dynamics. Earth and Planetary Science Letters, 264, 402–419.

Cashman, K.V., and Sparks, R.S.J. (2013) How volcanoes work: A 25 year perspective. Geological Society of America Bulletin, 125, 664–690.

Cashman, K.V., Sparks, R.S.J., and Blundy, J.D. (2017) Vertically extensive and unstable magmatic systems: A unified view of igneous processes. Science, 355, eaag3055.

Clark, P.J., and Evans, F.C. (1954) Distance to nearest neighbor as a measure of spatial relationships in populations. Ecology, 35, 445–453.

Coint, N., Barnes, C.G., Yoshinobu, A.S., Barnes, M.A., and Buck, S. (2013) Use of trace element abundances in augite and hornblende to determine the size, connectivity, timing, and evolution of magma batches in a tilted batholith. Geosphere, 9, 1747–1765.

Cortecci, G., Del Moro, A., Leone, G., and Pardini, G.C. (1979) Correlation between strontium and oxygen isotopic compositions of rocks from the Adamello Massif (Northern Italy). Contributions to Mineralogy and Petrology, 68, 421–427.

Costa, F., Scaillet, B., and Pichavant, M. (2004) Petrological and experimental constraints on the pre-eruption conditions of Holocene Dacite from Volcán San Pedro (36°S, Chilean Andes) and the importance of sulphur in silicic subduction-related magmas. Journal of Petrology, 45, 855–881.

Cox, K.G., Bell, J.D., and Pankhurst, R.J. (1979) The Interpretation of Igneous Rocks, 450 p. George, Allen and Unwin, London.

Davis, R.H., and Acrivos, A. (1985) Sedimentation of noncolloidal particles at low Reynolds numbers. Annual Review of Fluid Mechanics, 17, 91–118.

Davis, J.W., Coleman, D.S., Gracely, J.T., Gaschnig, R., and Stearns, M. (2012) Magma accumulation rates and thermal histories of plutons of the Sierra Nevada batholith, CA. Contributions to Mineralogy and Petrology, 163, 449–465.

de Silva, S.L., and Wolff, J.A. (1995) Zoned magma chambers: the influence of magma chamber geometry on sidewall convective fractionation. Journal of Volcanology and Geothermal Research, 65, 111–118.

Deering, C.D., and Bachmann, O. (2010) Trace element indicators of crystal accumulation in silicic igneous rocks. Earth and Planetary Science Letters, 297, 324–331.

Del Moro, A., Ferrara, G., Tonarini, S., and Callegari, E. (1983a) Rb-Sr systematics on rocks from the Adamello batholith (Southern Alps). Mem Soc Geol It, 26, 261–284.

Del Moro, A., Pardini, G., Quercioli, C., Villa, I.M., and Callegari, E. (1983b) Rb/Sr and K/Ar chronology of Adamello granitoids, Southern Alps. Memorie della

Società Geologica Italiana, 26, 285–299.
Dufek, J., and Bachmann, O. (2010) Quantum magmatism: Magmatic compositional gaps generated by melt-crystal dynamics. Geology, 38, 8, 687–690.
Eddy, M.P., Bowring, S.A., Miller, R.B., and Tepper, J.H. (2016) Rapid assembly and crystallization of a fossil large-volume silicic magma chamber. Geology, 44, 331–334.
Ehlers, E.G. (1972) The Interpretation of Geological Phase Diagrams, 280 p. Freeman, San Francisco.
Floess, D., and Baumgartner, L.P. (2015) Constraining magmatic fluxes through thermal modelling of contact metamorphism. Geological Society, London, Special Publications, 422, SP422.8.
Forni, F., Bachmann, O., Mollo, S., De Astis, G., Gelman, S.E., and Ellis, B.S. (2016) The origin of a zoned ignimbrite: Insights into the Campanian Ignimbrite magma chamber (Campi Flegrei, Italy). Earth and Planetary Science Letters, 449, 259–271.
Frelinger, S.N., Ledvina, M.D., Kyle, J.R., and Zhao, D. (2015) Scanning electron microscopy cathodoluminescence of quartz: Principles, techniques and applications in ore geology. Ore Geology Reviews, 65, 840–852.
Gelman, S.E., Deering, C.D., Bachmann, O., Huber, C., and Gutiérrez, F.J. (2014) Identifying the crystal graveyards remaining after large silicic eruptions. Earth and Planetary Science Letters, 403, 299–306.
Ginibre, C., Kronz, A., and Wörner, G. (2002) High-resolution quantitative imaging of plagioclase composition using accumulated backscattered electron images: new constraints on oscillatory zoning. Contributions to Mineralogy and Petrology, 142, 436–448.
Ginibre, C., Wörner, G., and Kronz, A. (2007) Crystal zoning as an archive for magma evolution. Elements, 3, 261–266.
Glazner, A.F., Coleman, D.S., and Bartley, J.M. (2008) The tenuous connection between high-silica rhyolites and granodiorite plutons. Geology, 36, 183–186.
Glazner, A.F., Coleman, D.S., and Mills, R.D. (2015) The Volcanic-Plutonic Connection, pp. 1–22. Springer.
Götze, J. (2012) Application of cathodoluminescence microscopy and spectroscopy in geosciences. Microscopy and Microanalysis, 18, 1270–1284.
Graeter, K.A., Beane, R.J., Deering, C.D., Gravley, D., and Bachmann, O. (2015) Formation of rhyolite at the Okataina Volcanic Complex, New Zealand: New insights from analysis of quartz clusters in plutonic lithics. American Mineralogist, 100, 1778–1789.
Guillong, M., Meier, D.L., Allan, M.M., Heinrich, C.A., and Yardley, B.W. (2008) Appendix A6: SILLS: A MATLAB-based program for the reduction of laser ablation ICP-MS data of homogeneous materials and inclusions. Mineralogical Association of Canada Short Course, 40, 328–333.
Gutiérrez, F., Payacán, I., Gelman, S.E., Bachmann, O., and Parada, M.A. (2013) Late-stage magma flow in a shallow felsic reservoir: Merging the anisotropy of magnetic susceptibility record with numerical simulations in La Gloria Pluton, central Chile. Journal of Geophysical Research: Solid Earth, 118, 1984–1998.
Hersum, T. (2009) Consequences of crystal shape and fabric on anisotropic permeability in magmatic mush. Contributions to Mineralogy and Petrology, 157, 285–300.
Hielscher, R., and Schaeben, H. (2008) A novel pole figure inversion method: specification of the MTEX algorithm. Journal of Applied Crystallography, 41, 1024–1037.
Higgins, M.D. (1991) The origin of laminated and massive anorthosite, Sept Iles layered intrusion, Quebec, Canada. Contributions to Mineralogy and Petrology, 106, 340–354.
——— (2000) Measurement of crystal size distributions. American Mineralogist, 85, 1105–1116.
——— (2002) Closure in crystal size distributions (CSD), verification of CSD calculations, and the significance of CSD fans. American Mineralogist, 87, 171–175.
——— (2016) Quantitative investigation of felsic rock textures using cathodoluminescence images and other techniques. Lithos, 277, 259–268.
Hildreth, W. (2004) Volcanological perspectives on Long Valley, Mammoth Mountain, and Mono Craters: several contiguous but discrete systems. Journal of Volcanology and Geothermal Research, 136, 169–198.
Hildreth, W., and Fierstein, J. (2000) Katmai volcanic cluster and the great eruption of 1912. Geological Society of America Bulletin, 112, 1594–1620.
Holder, M.T. (1979) An emplacement mechanism for post-tectonic granites and its implications for their geochemical features. In M.P. Atherton and J. Tarney, Eds., Origin of Granite Batholiths, p. 116–128. Birkhäuser, Boston.
Huber, C., Bachmann, O., and Dufek, J. (2012) Crystal-poor versus crystal-rich ignimbrites: A competition between stirring and reactivation. Geology, 40, 115–118.
Hunter, R.H. (1996) Texture development in cumulate rocks. In R.G. Cawthorn, Ed., Developments in Petrology (Elsevier), 15, 77–101.
Hürlimann, N., Müntener, O., Ulmer, P., Nandedkar, R., Chiaradia, M., and Ovtcharova, M. (2016) Primary magmas in continental arcs and their differentiated products: Petrology of a post-plutonic dyke suite in the Tertiary Adamello Batholith (Alps). Journal of Petrology, 57, 495–534.
Irvine, T.N. (1982) Terminology for layered intrusions. Journal of Petrology, 23, 127–162.
Jackson, M.D., Cheadle, M.J., and Atherton, M.P. (2003) Quantitative modeling of granitic melt generation and segregation in the continental crust. Journal of Geophysical Research: Solid Earth, 108, 2332.
Jerram, D.A., and Higgins, M.D. (2007) 3D analysis of rock textures: Quantifying igneous microstructures. Elements, 3, 239–245.
Jerram, D.A., Cheadle, M.J., Hunter, R.H., and Elliott, M.T. (1996) The spatial distribution of grains and crystals in rocks. Contributions to Mineralogy and Petrology, 125, 60–74.
Jerram, D.A., Cheadle, M., and Philpotts, A.R. (2003) Quantifying the building blocks of igneous rocks: are clustered crystal frameworks the foundation? Journal of Petrology, 44, 2033–2051.
Johannes, W. (1984) Beginning of melting in the granite system Qz-Or-Ab-An-H_2O. Contributions to Mineralogy and Petrology, 86, 264–273.
Johannes, W., and Holtz, F. (1996) Petrogenesis and Experimental Petrology of Granitic Rocks, 335 p. Springer.
John, B.E., and Blundy, J.D. (1993) Emplacement-related deformation of granitoid magmas, southern Adamello Massif, Italy. Geological Society of America Bulletin, 105, 1517–1541.
John, B.E., and Stünitz, H. (1997) Magmatic fracturing and small-scale melt segregation during pluton emplacement: Evidence from the Adamello massif (Italy). In J.L. Bouchez, D.H.W. Hutton, and W.E. Stephens, Eds., Granite: From Segregation of Melt to Emplacement Fabrics, pp. 55–74. Springer.
Kagami, H., Ulmer, P., Hansmann, W., Dietrich, V., and Steiger, R.H. (1991) Nd-Sr isotopic and geochemical characteristics of the southern Adamello (northern Italy) intrusives: Implications for crustal versus mantle origin. Journal of Geophysical Research: Solid Earth, 96, 14331–14346.
Kesley, C.H. (1965) Calculation of the CIPW norm. Mineralogical Magazine, 34, 376–282.
Lapworth, T., Wheeler, J., and Prior, D.J. (2002) The deformation of plagioclase investigated using electron backscatter diffraction crystallographic preferred orientation data. Journal of Structural Geology, 24, 387–399.
Laubscher, H.P. (1983) The late Alpine (Periadriatic) intrusions and the Insubric line. Memorie della Società Geologica Italiana, 26, 21–30.
Launeau, P., and Robin, P.-Y.F. (1996) Fabric analysis using the intercept method. Tectonophysics, 267, 91–119.
Launeau, P., Archanjo, C.J., Picard, D., Arbaret, L., and Robin, P. (2010) Two- and three-dimensional shape fabric analysis by the intercept method in grey levels. Tectonophysics, 492, 1, 230–239.
Lee, C.T.A., and Morton, D.M. (2015) High silica granites: Terminal porosity and crystal settling in shallow magma chambers. Earth and Planetary Science Letters, 409, 23–31.
Leuthold, J., Müntener, O., Baumgartner, L.P., and Putlitz, B. (2014) Petrological constraints on the recycling of mafic crystal mushes and intrusion of braided sills in the Torres del Paine Mafic Complex (Patagonia). Journal of Petrology, 55, 917–949.
Liebske, C. (2015) iSpectra: An open source toolbox for the analysis of spectral images recorded on scanning electron microscopes. Microscopy and Microanalysis, 21, 1006–1016.
Lipman, P.W. (2007) Incremental assembly and prolonged consolidation of Cordilleran magma chambers: Evidence from the Southern Rocky Mountain volcanic field. Geosphere, 3, 42.
Lipman, P.W., and Bachmann, O. (2015) Ignimbrites to batholiths: Integrating perspectives from geological, geophysical, and geochronological data. Geosphere, 11, 1–39.
Macera, P., Ferrara, G., Pescia, A., and Callegari, E. (1983) A geochemical study on the acid and basic rocks of the Adamello batholith. Mem Soc Geol Ital, 26, 223–259.
Mainprice, D., Bachmann, F., Hielscher, R., and Schaeben, H. (2014) Descriptive tools for the analysis of texture projects with large datasets using MTEX: Strength, symmetry and components. In D.R. Faulkner, E. Mariani, and J. Mecklenburgh, Eds., Rock Deformation from Field, Experiments and Theory: A Volume in Honour of Ernie Rutter, vol. 8. Geological Society, London.
Martel, C., Pichavant, M., Holtz, F., Scaillet, B., Bourdier, J.-L., and Traineau, H. (1999) Effects of f_{O_2} and H_2O on andesite phase relations between 2 and 4 kbar. Journal of Geophysical Research: Solid Earth, 104, 29453–29470.
Martin, S., and Macera, P. (2014) Tertiary volcanism in the Italian Alps (Giudicarie fault zone, NE Italy): Insight for double alpine magmatic arc. Italian Journal of Geosciences, 133, 63–84.
Mauler, A., Godard, G., and Kunze, K. (2001) Crystallographic fabrics of omphacite, rutile and quartz in Vendée eclogites (Armorican Massif, France). Consequences for deformation mechanisms and regimes. Tectonophysics, 342, 81–112.
Mayer, A., Cortiana, G., Dal Piaz, G.V., Deloule, E., De Pieri, R., and Jobstraibizer, P. (2003) U-Pb single zircon ages of the Adamello batholith, Southern Alps. Memorie di Scienze Geologiche, 55, 151–167.
McCarthy, T.S., and Groves, D.I. (1979) The Blue Tier Batholith, northeastern Tasmania. Contributions to Mineralogy and Petrology, 71, 193–209.
McKenzie, D. (1984) The generation and compaction of partially molten rock.

Journal of Petrology, 25, 713–765.
——— (1985) The extraction of magma from the crust and mantle. Earth and Planetary Science Letters, 74, 81–91.
Meurer, W.P., and Boudreau, A.E. (1998a) Compaction of igneous cumulates part I: Geochemical consequences for cumulates and liquid fractionation trends. The Journal of Geology, 106, 281–292.
——— (1998b) Compaction of igneous cumulates part II: Compaction and the development of igneous foliations. The Journal of Geology, 106, 293–304.
Miller, C.F., and Miller, J.S. (2002) Contrasting stratified plutons exposed in tilt blocks, Eldorado Mountains, Colorado River Rift, NV, USA. Lithos, 61, 209–224.
Miller, C.F., Watson, E.B., and Harrison, T.M. (1988) Perspectives on the source, segregation and transport of granitoid magmas. Earth and Environmental Science Transactions of the Royal Society of Edinburgh, 79, 135–156.
Mills, R.D., and Coleman, D.S. (2013) Temporal and chemical connections between plutons and ignimbrites from the Mount Princeton magmatic center. Contributions to Mineralogy and Petrology, 165, 961–980.
Müller, A., Wiedenbeck, M., van den Kerkhof, A.M., Kronz, A., and Simon, K. (2003) Trace elements in quartz-a combined electron microprobe, secondary ion mass spectrometry, laser-ablation ICP-MS, and cathodoluminescence study. European Journal of Mineralogy, 15, 4, 747–763.
Müller, A., van den Kerkhof, A.M., Behr, H.J., Kronz, A., and Koch-Müller, M. (2010) The evolution of late-Hercynian granites and rhyolites documented by quartz—a review. Geological Society of America Special Papers, 472, 185–204.
Namur, O., and Charlier, B. (2012) Efficiency of compaction and compositional convection during mafic crystal mush solidification: the Sept Iles layered intrusion, Canada. Contributions to Mineralogy and Petrology, 163, 1049–1068.
Nandedkar, R. (2014) Evolution of hydrous mantle-derived calc-alkaline liquids by fractional crystallization at 0.7 and 0.4 GPa—An experimental study. Ph.D. thesis, ETH Zürich.
Nandedkar, R.H., Ulmer, P., and Müntener, O. (2014) Fractional crystallization of primitive, hydrous arc magmas: an experimental study at 0.7 GPa. Contributions to Mineralogy and Petrology, 167(6), 1015.
Nicolas, A. (1992) Kinematics in magmatic rocks with special reference to gabbros. Journal of Petrology, 33, 891–915.
Otamendi, J.E., Tiepolo, M., Walker, B.A., Cristofolini, E.A., and Tibaldi, A.M. (2016) Trace elements in minerals from mafic and ultramafic cumulates of the central Sierra de Valle Fértil, Famatinian arc, Argentina. Lithos, 240, 355–370.
Paterson, S.R., Vernon, R.H., and Tobisch, O.T. (1989) A review of criteria for the identification of magmatic and tectonic foliations in granitoids. Journal of Structural Geology, 11, 349–363.
Paterson, S.R., Okaya, D., Memeti, V., Economos, R., and Miller, R.B. (2011) Magma addition and flux calculations of incrementally constructed magma chambers in continental margin arcs: Combined field, geochronologic, and thermal modeling studies. Geosphere, 7, 1439–1468.
Pennacchioni, G., Di Toro, G., Brack, P., Menegon, L., and Villa, I.M. (2006) Brittle–ductile–brittle deformation during cooling of tonalite (Adamello, Southern Italian Alps). Tectonophysics, 427, 171–197.
Perugini, D., Poli, G., and Valentini, L. (2005) Strange attractors in plagioclase oscillatory zoning: Petrological implications. Contributions to Mineralogy and Petrology, 149, 482–497.
Petford, N. (2003) Rheology of granitic magmas during ascent and emplacement. Annual Review of Earth and Planetary Sciences, 31, 399–427.
Philpotts, A.R., and Philpotts, D.E. (2005) Crystal-mush compaction in the Cohassett flood-basalt flow, Hanford, Washington. Journal of Volcanology and Geothermal Research, 145, 192–206.
Philpotts, A.R., Carroll, M., and Hill, J.M. (1996) Crystal-mush compaction and the origin of pegmatitic segregation sheets in a thick flood-basalt flow in the Mesozoic Hartford Basin, Connecticut. Journal of Petrology, 37, 811–836.
Philpotts, A.R., Shi, J., and Brustman, C. (1998) Role of plagioclase crystal chains in the differentiation of partly crystallized basaltic magma. Nature, 395, 343–346.
Philpotts, A.R., Brustman, C.M., Shi, J., Carlson, W.D., and Denison, C. (1999) Plagioclase-chain networks in slowly cooled basaltic magma. American Mineralogist, 84, 1819–1829.
Pistone, M., Arzilli, F., Dobson, K.J., Cordonnier, B., Reusser, E., Ulmer, P., Marone, F., Whittington, A.G., Mancini, L., Fife, J.L., and others. (2015) Gas-driven filter pressing in magmas: Insights into in-situ melt segregation from crystal mushes. Geology, 43, 699–702.
Piwinskii, A.J. (1968) Experimental studies of igneous rock series Central Sierra Nevada Batholith, California. The Journal of Geology, 76, 548–570.
——— (1973) Experimental studies of granitoids from the Central and Southern Coast Ranges, California. Tschermaks Mineralogische und Petrographische Mitteilungen, 20, 107–130.
Piwinskii, A.J., and Wyllie, P.J. (1968) Experimental studies of igneous rock series: a zoned pluton in the Wallowa batholith, Oregon. The Journal of Geology, 76, 205–234.
Prior, D.J., Boyle, A.P., Brenker, F., Cheadle, M.C., Day, A., Lopez, G., Peruzzo, L., Potts, G.J., Reddy, S., Spiess, R., and others. (1999) The application of electron backscatter diffraction and orientation contrast imaging in the SEM to textural problems in rocks. American Mineralogist, 84, 1741–1759.
Putirka, K.D., Canchola, J., Rash, J., Smith, O., Torrez, G., Paterson, S.R., and Ducea, M.N. (2014) Pluton assembly and the genesis of granitic magmas: Insights from the GIC pluton in cross section, Sierra Nevada Batholith, California. American Mineralogist, 99, 1284–1303.
Reubi, O., and Blundy, J. (2009) A dearth of intermediate melts at subduction zone volcanoes and the petrogenesis of arc andesites. Nature, 461, 1269–1273.
Sahagian, D.L., and Proussevitch, A.A. (1998) 3D particle size distributions from 2D observations: Stereology for natural applications. Journal of Volcanology and Geothermal Research, 84, 173–196.
Scaillet, B., and Evans, B.W. (1999) The 15 June 1991 Eruption of Mount Pinatubo. I. Phase equilibria and pre-eruption P–T–f_{O_2}–f_{H_2O} conditions of the dacite magma. Journal of Petrology, 40, 381–411.
Schaltegger, U., Brack, P., Ovtcharova, M., Peytcheva, I., Schoene, B., Stracke, A., Marocchi, M., and Bargossi, G. (2009) Zircon and titanite recording 1.5 million years of magma accretion, crystallization and initial cooling in a composite pluton (Southern Adamello Batholith, Northern Italy). Earth and Planetary Science Letters, 286, 208–218.
Schmidt, M.W., and Thompson, A.B. (1996) Epidote in calcalkaline magmas; an experimental study of stability, phase relationships, and the role of epidote in magmatic evolution. American Mineralogist, 81, 462–474.
Schoene, B., Schaltegger, U., Brack, P., Latkoczy, C., Stracke, A., and Günther, D. (2012) Rates of magma differentiation and emplacement in a ballooning pluton recorded by U–Pb TIMS-TEA, Adamello batholith, Italy. Earth and Planetary Science Letters, 355–356, 162–173.
Schwartz, A.J., Kumar, M., Adams, B.L., and Field, D.P., Eds. (2009) Electron Backscatter Diffraction in Materials Science. Springer, Boston.
Schwindinger, K.R., and Anderson, A.T.J. (1989) Synneusis of Kilauea Iki olivines. Contributions to Mineralogy and Petrology, 103, 187–198.
Shirley, D.N. (1986) Compaction of igneous cumulates. The Journal of Geology, 795–809.
Sisson, T.W., and Bacon, C.R. (1999) Gas-driven filter pressing in magmas. Geology, 27, 613.
Skemer, P., Katayama, I., Jiang, Z., and Karato, S.I. (2005) The misorientation index: Development of a new method for calculating the strength of lattice-preferred orientation. Tectonophysics, 411, 157–167.
Słaby, E., and Götze, J. (2004) Feldspar crystallization under magma-mixing conditions shown by cathodoluminescence and geochemical modelling-a case study from the Karkonosze pluton (SW Poland). Mineralogical Magazine, 68, 561–577.
Słaby, E., De Campos, C.P., Majzner, K., Simon, K., Gros, K., Moszumańska, I., and Jokubauskas, P. (2016) Feldspar megacrysts from the Santa Angélica composite pluton—Formation/transformation path revealed by combined CL, Raman and LA-ICP-MS data. Lithos, 277, 269–283.
Spera, F.J., Oldenburg, C.M., Christensen, C., and Todesco, M. (1995) Simulations of convection with crystallization in the system $KAlSi_2O_6$-$CaMgSi_2O_6$: Implications for compositionally zoned magma bodies. American Mineralogist, 80, 1188–1207.
Streck, M.J. (2014) Evaluation of crystal mush extraction models to explain crystal-poor rhyolites. Journal of Volcanology and Geothermal Research, 284, 79–94.
Streck, M.J., and Grunder, A.L. (2007) Phenocryst-poor rhyolites of bimodal, tholeiitic provinces: the Rattlesnake Tuff and implications for mush extraction models. Bulletin of Volcanology, 70, 385–401.
Tappa, M.J., Coleman, D.S., Mills, R.D., and Samperton, K.M. (2011) The plutonic record of a silicic ignimbrite from the Latir volcanic field, New Mexico. Geochemistry, Geophysics, Geosystems, 12, Q10011.
Taylor, H.P. (1980) The effects of assimilation of country rocks by magmas on $^{18}O/^{16}O$ and $^{87}Sr/^{86}Sr$ systematics in igneous rocks. Earth and Planetary Science Letters, 47, 243–254.
Tegner, C., Thy, P., Holness, M.B., Jakobsen, J.K., and Lesher, C.E. (2009) Differentiation and compaction in the Skaergaard Intrusion. Journal of Petrology, 50, 813–840.
Thompson, A.B., Matile, L., and Ulmer, P. (2002) Some thermal constraints on crustal assimilation during fractionation of hydrous, mantle-derived magmas with examples from central Alpine batholiths. Journal of Petrology, 43, 403–422.
Tiepolo, M., Tribuzio, R., and Langone, A. (2011) High-Mg andesite petrogenesis by amphibole crystallization and ultramafic crust assimilation: Evidence from Adamello hornblendites (Central Alps, Italy). Journal of Petrology, 52, 1011–1045.
Turnbull, R., Weaver, S., Tulloch, A., Cole, J., Handler, M., and Ireland, T. (2010) Field and geochemical constraints on mafic–felsic interactions, and processes in high-level arc magma chambers: An example from the Halfmoon Pluton, New Zealand. Journal of Petrology, 51, 1477–1505.
Tuttle, O.F., and Bowen, N.L. (1958) Origin of granite in the light of experimental studies in the system $NaAlSi_3O_8$–$KAlSi_3O_8$–SiO_2–H_2O. Geological Society of America Memoirs, 74, 1–146.
Ulmer, P., Callegari, E., and Sonderegger, U.C. (1983) Genesis of the mafic and ultramafic rocks and their genetical relations to the tonalitic-trondhjemitic

granitoids of the southern part of the Adamello batholith (Northern Italy). Memorie della Società Geologica Italiana, 26, 171–222.
Vance, J.A. (1969) On synneusis. Contributions to Mineralogy and Petrology, 24, 7–29.
Vasyukova, O.V., Kamenetsky, V.S., Goemann, K., and Davidson, P. (2013) Diversity of primary CL textures in quartz from porphyry environments: implication for origin of quartz eyes. Contributions to Mineralogy and Petrology, 166, 1253–1268.
Vigneresse, J.L., Barbey, P., and Cuney, M. (1996) Rheological transitions during partial melting and crystallization with application to felsic magma segregation and transfer. Journal of Petrology, 37, 1579–1600.
Vollmer, F.W. (1990) An application of Eigenvalue methods to structural domain analysis. Geological Society of America Bulletin, 102, 786–791.
von Platen, H. (1965) Kristallisation granitischer Schmelzen. Beiträge zur Mineralogie und Petrographie, 11, 334–381.
Wager, L.R. (1960) The major element variation of the layered series of the Skaergaard intrusion and a re-estimation of the average composition of the hidden layered series and of the successive residual magmas. Journal of Petrology, 1, 364–398.
Wager, L.R., and Brown, G.M. (1968) Layered Igneous Rocks. Oliver & Boyd, Edinburgh.
Walker, B.A., Bergantz, G.W., Otamendi, J.E., Ducea, M.N., and Cristofolini, E.A. (2015) A MASH zone revealed: The mafic complex of the Sierra Valle Fértil. Journal of Petrology, 56, 1863–1896.
Weinberg, R.F. (2006) Melt segregation structures in granitic plutons. Geology, 34, 305–308.
Wheeler, J., Prior, D., Jiang, Z., Spiess, R., and Trimby, P. (2001) The petrological significance of misorientations between grains. Contributions to Mineralogy and Petrology, 141, 109–124.
Wickham, S.M. (1987) The segregation and emplacement of granitic magmas. Journal of the Geological Society, 144, 281–297.
Wiebe, R.A., Wark, D.A., and Hawkins, D.P. (2007) Insights from quartz cathodoluminescence zoning into crystallization of the Vinalhaven granite, coastal Maine. Contributions to Mineralogy and Petrology, 154, 439–453.
Žák, J., Verner, K., and Týcová, P. (2008) Grain-scale processes in actively deforming magma mushes: New insights from electron backscatter diffraction (EBSD) analysis of biotite schlieren in the Jizera granite, Bohemian Massif. Lithos, 106, 309–322.

Manuscript received November 18, 2016
Manuscript accepted August 11, 2017
Manuscript handled by Calvin Barnes